In-situ X-ray tomographic imaging of microstructure evolution of fly ash and slag particles in alkali-activated fly ash-slag paste

Guohao Fang [a, b], Qiang Wang [c], Mingzhong Zhang [b, *]

[a] Institute for Advanced Study, Shenzhen University, Shenzhen, 518060, China

[b] Department of Civil, Environmental and Geomatic Engineering, University College London, London, WC1E 6BT, UK

[c] Department of Civil Engineering, Tsinghua University, Beijing, 100084, China

Abstract: This paper presents an in-situ investigation of the microstructure evolution of fly ash and slag particles in alkali-activated fly ash-slag paste using X-ray microcomputed tomography. Results indicate that the dissolution of fly ash and slag particles is not uniform especially for the particles with large size due to the heterogeneous distribution of chemical composition and initial defects. The dissolution of the particles with small size is faster than that of large particles owing to the relatively high specific area. The formation of reaction products (i.e., inner products) is mostly accumulated within the boundary of original particles, which become a barrier to prevent the further dissolution of unreacted particles. The fly ash-slag interaction in terms of microstructure evolution is not obvious at early ages (1 – 3 d) but becomes apparent at later ages (7 – 28 d), which can be attributed to the continuous transport of dissolved ions between fly ash and slag.

Keywords: Alkali-activated materials; Microstructure; In-situ imaging; Computed tomography (CT); 3D reconstruction

1. Introduction

Alkali-activated fly ash-slag (AAFS) is considered as a promising alternative binder to Portland cement (PC) because of its environmental benefits (i.e. low CO_2 emission and low consumption of natural sources) and superior engineering properties under ambient curing conditions [1-4]. AAFS paste is produced by the chemical reaction between alkaline activators and aluminosilicate source materials, i.e. fly ash and slag, which leads to the microstructure evolution and motivates the development of performance [5-8]. The dissolution of fly ash and slag particles and the subsequent formation of binding gels are crucial features controlling the development of microscopic and macroscopic performance of AAFS system [9, 10]. It was reported that the dissolution behaviour of fly ash and slag particles depends on the relationship between forward and backward reactions leading to equilibrium [11]. The forward reaction is about the breaking of surface bonds (e.g. Si-O-Si and Al-O-Al bonds in fly ash; Ca-O and Si-O-Si bonds in slag) and the dissolution of soluble species (e.g. Si and Al species) under the activation of alkaline activators, while the backward reaction is related to the reaction between soluble species and the formation of binding gels [11]. A balance between the forward dissolution rate and the backward reaction rate of a particle would

* Corresponding author. E-mail address: mingzhong.zhang@ucl.ac.uk (M. Zhang)

promote the formation of desirable phases, resulting in a good matrix integrity and durability [12]. The forward and backward reactions would control the release of different species and accordingly affect the synthesis and structure development of binding gels. The rapid release of Al species would hinder the dissolution of Si species and result in the formation of high crystalline zeolite products, while more amorphous products prefer to form with the slower releasing rate of Al species [13]. Additionally, the microstructure evolution of fly ash and slag particles is dependent on their inherent characteristics, such as particle size and mineral compositions [14, 15]. Brouwers and Van Eijk [14] applied a shrinking core model to simulate the dissolution and reaction behaviour of fly ash particle and concluded that the solubility and reaction rate of fly ash particle are proportional to its glass content. Fernandez-Jimenez et al. [15] found that the dissolution of fly ash particle in the paste matrix is not uniform but varies locally from one region to another, depending on the size of fly ash particle and local chemistry (e.g. pH value). Furthermore, the fly ash-to-slag ratio and the type and concentration of alkaline activator would also affect the microstructure evolution of source particles [16, 17]. The Ca species released from the dissolution of slag particles would enhance the dissolution of fly ash particles and the formation of geopolymer gels [16]. The alkaline activator with a high pH value would promote the dissolution of Si and Al species from fly ash and slag particles, but it is not favourable for the dissolution of Ca species [17].

Although the dissolution of fly ash and slag particles in AAFS system has been investigated for more than a decade, the reaction mechanisms have not been fully understood due to lack of in-situ characterisation, e.g., in-situ microstructure evolution of fly ash and slag particles and reaction products during the dissolution process. Scanning electron microscopy (SEM), energy dispersive spectrometry (EDS) and transmission electron microscopy (TEM) are commonly used to characterise the microstructural development of fly ash and slag particles in AAFS mixes [16, 18], which can provide valuable two-dimensional (2D) information for evaluating the microstructure evolution of particles [19, 20]. However, the preparation of samples for these tests requires pre-treatment such as cutting, grinding and polishing that may cause destruction of the samples and the in-situ monitoring of three-dimensional (3D) microstructure development cannot be achieved using these techniques. To better understand the particle dissolution process and the formation process of reaction products, it is vital to find a testing method that can non-destructively track the location, morphology and density changes of the dissolution particles and reaction products.

X-ray microcomputed tomography (XCT) provides a potential opportunity for in-situ characterisation of microstructure evolution of fly ash and slag particles in AAFS, owing to the penetration ability of X-ray to pass through the thick and opaque objects [21, 22]. Based on the image reconstruction technique, the internal 3D structure of a testing sample can be qualitatively and quantitatively characterised [23]. Over the past decades, XCT has been successfully used to

non-destructively explore the hydration and microstructure of cementitious materials, such as time-dependent reaction process, dissolution of cement particles, subsequent formation and development of reaction products, and pore structure features [24-30]. Wang et al. [31] applied XCT to investigate the cement hydration and 3D microstructure development of cement mixes at different curing ages. Gastaldi et al. [25] utilized XCT to measure the grey level histograms during cement hydration and characterise the evolution of hydration products. More recently, Hu et al. [24] used this technique to monitor the 3D microstructure evolution of C_3S particle before and after reaction (2.5 h of hydration), which provides direct insights into the morphological change of the particle (both surface and interior) and surrounding hydration products.

In recent years, several attempts have been made to characterise the microstructure evolution of alkali-activated materials with a particular focus on pore structure development using XCT [32-34]. Provis et al. [32] provided the first ever systematic 3D analysis of pore network geometry in AAFS paste in terms of porosity, pore tortuosity and connectivity by means of XCT. Zhu et al. [35] used the same method to measure the pore connectivity in alkali-activated slag (AAS) paste, which agrees well with the results obtained from electrical response measurements. However, the research on the use of XCT to detect the changes in the microstructure of fly ash or slag particles and the surrounding reaction products is extremely limited. To date, only one study [36] presented the XCT characterisation of the binding between geopolymer gel and unreacted fly ash particle and the 3D pore structure of the aluminosilicate geopolymer gel in alkali-activated fly ash (AAF) paste. The XCT technique proves very effective to gain a 3D view of nano-porous inorganic materials, which helps better understand the reaction process and microstructure development of AAF and optimise its mix proportions. Nevertheless, the existing studies are limited to the qualitative analysis of particle structure, while the relevant quantitative characterisation as well as the time-dependent evolution of particle structure have not been addressed. Furthermore, the effects of particle size and structure on the microstructural evolution of fly ash and slag particles in AAFS still remain unknown. It is vital to investigate the 3D microstructural evolution of fly ash and slag particles in AAFS mixes, which would provide a comprehensive understanding of the reaction mechanisms of fly ash and slag particles as well as microstructural evolution and property development of AAFS paste.

In this study, a systematic analysis based on in-situ XCT imaging is conducted to monitor the microstructural evolution of individual fly ash and slag particles with different sizes and structures (i.e., solid and hollow) in AAFS paste cured at ambient temperature and gain new insights into the reaction mechanisms of AAFS systems. The high-resolution reconstruction was performed to visualise the time-dependent 3D microstructures of fly ash and slag particles in AAFS paste from 1 d to 28 d, indicating the morphology changes on the surface and interior of particles and the spatial

distribution of reaction products, based on which the reaction process in terms of reaction depth, reaction degree and reaction rate was estimated. For comparison, SEM-EDS analysis was also undertaken, the results of which were used to validate the in-situ XCT findings and gain an in-depth understanding of reaction mechanisms of AAFS.

2. Experimental program

2.1. Raw materials and mix proportion

Low-calcium fly ash and ground granulated blast-furnace slag were selected as precursors (P) in this study, the chemical compositions and particle distribution of which are shown in Tables 1 and 2, respectively. The alkaline activator (AL) is composed of sodium hydroxide (SH) solution with molarity of 10 and sodium silicate (SS) solution with modulus (SiO_2:Na_2O ratio) of 2.0. The modified polycarboxylate-based superplasticizer (SP) (Sika®ViscoFlow®2000, Sika, UK) was used to improve the workability of AAFS paste as per a previous study [37]. Regarding the used mix proportion, the mass ratios of fly ash/slag, AL/P, SS/SH and SP/P were set as 3, 0.45, 2.0 and 0.01, respectively, based on the authors' previous research [37] and the literature [38-40], which can meet the performance criteria in terms of workability [41], setting time [42] and compressive strength [43]. The mix quantity of AAFS paste was presented in Table 3.

2.2. Sample preparation

Considering the above mix proportion, fly ash and slag were dry mixed firstly for 2 min, followed by another 3 min mixing with the addition of SS, SH and SP. The fresh paste was then prepared and cast into the plastic cuboid moulds with size of 1 × 1 × 10 mm (for XCT test) and the plastic cuboid moulds with size of 20 × 20 × 20 mm (for BSEM/EDS test). Afterwards, the moulds were stored in a standard curing room (20 ± 2 °C, 95% RH). The plastic cuboid mould was continuously cured in the same curing room, except taken out for XCT testing at 1, 3, 7 and 28 d.

Regarding the cube moulds, the samples were demoulded after curing of 24 h and stored in the same curing room (20 ± 2 °C, 95% RH) until the days of testing, i.e., 1, 3, 7 and 28 d. At each curing age, the samples were cut using the low-speed diamond saw to acquire the small specimens with size of 2 × 20 × 20 mm. The specimens were then placed in the isopropanol solution for 2 d to stop the chemical reaction of binder, followed by a 2-d drying process in the vacuum drying dish (20 ± 2 °C). Lastly, the specimens were well polished to provide a smooth and flat surface for BSEM/EDS test. More details about the preparation of specimens can be found in a previous study [44].

2.3.Test methods

2.3.1. X-ray microcomputed tomography (XCT) test

XCT scans were performed with the assistant of XRadia Micro XCT-400 scope (Zeiss, Germany). Fig. 1 shows the XCT system consisting of a microfocus X-ray emitter, a rotation stage,

and an image intensifier detector with charge-coupled device (CCD) camera. A special sample stage was used to tightly hold the testing sample, which can make sure the sample was set in the same position at each test. XCT scans were performed at 59 kV and 150 μA, while the magnification was 0.4×. The total scanning time for each test is about 7 h, where 2501 projections (angle step of 0.144° from -180° to 180°) were acquired with a 10 s exposure time per projection. The field of view was 1.5 mm (x = y = z) and the spatial resolution (voxel size) was 1.56 μm (x = y = z).

2.3.2. Backscattered electron microscopy (BSEM)/energy dispersive spectrometry (EDS) test

The environmental scanning electron microscopic (FEI, QUANTA FEG 450, USA) equipped with BSEM and EDS was used to characterise the morphology and chemical composition of AAFS paste. The surface of testing sample was coated with a layer of carbon under vacuum to improve the conductivity for BSEM and EDS tests. The working distance was set as 10 mm with an acceleration voltage of 15 kV and a spot size of 6 nm. The BSEM images with a pixel size of 20 nm were captured at a magnification of 4000×. For EDS analysis, the "line mode" with a dwell time of 200 ms at 100 testing points.

3. XCT image analysis

Fig. 2 shows a typical XCT image of AAFS paste, which is considered mathematically as a four-dimensional set, including the density and corresponding coordinates (x, y and z). As seen in Fig. 2a, each pixel in the image is characterised by its greyscale value ranging from 0 to 255 for an 8-bit image, attributing to the X-ray attenuation coefficient of the testing material which is associated with the density and atomic number of elements [45, 46]. Therefore, the grey level of XCT image can be used to identify different phases within AAFS paste. A multiphase composite made up of unreacted particles (fly ash and slag), reaction products and pore space can be characterised in the 2D slice image due to the difference of X-ray absorption. To analyse the multiple phases in 2D or 3D images, the XCT images were processed based on four steps: (i) denoising, (ii) segmentation, (iii) labelling, and (iv) quantification.

In the first step, image denoising was used to remove the noise of image data produced from the XCT test, which would help to improve the contrast between different phases. In this study, the non-local means filtering method was applied for this purpose because this method can preserve both edges and textures [47]. This method takes the mean value of image pixels weighted by the similarity between these pixels and the target pixel, which can achieve a better post-filtering clarity and a less loss of image details. Accordingly, the noise within the original greyscale image was successfully removed, as illustrated in Fig. 2b.

The image was then segmented into different phases (unreacted particles, reaction products and pores) through local thresholding, which is commonly used to determine the threshold value of a specified region locally based on the histogram of grey value in a neighbourhood rather than the

whole image [48]. This method can avoid the problem of overlapping of grey value distribution, in which case the voxels within the overlap region cannot be identified [21]. Since this study aims at in-situ monitoring the microstructure evolution of a specified area, e.g., fly ash and slag particles, the local thresholding method is suitable. Taking the fly ash particle as an example, the grey value of different phases can be identified with the assistance of local linear threshold (Fig. 2c). Herein, the red line across the fly ash particle indicates the location of grey value from point A to point H. The grey value is highest in the middle area of unreacted particle but drops sharply on the sides at the interface with paste matrix. The grey value of unreacted fly ash is measured to be 255, while that of paste mortar is in the range of 100-125. The reaction products accumulated at the interface between unreacted fly ash and paste matrix have a grey value between 125 and 255. The grey value under 100 represents the area of pores. The determination of threshold values should be adjusted locally according to different particles due to the inherently heterogeneity of fly ash and slag particles. The additional information on phase segmentation for different fly ash and slag particles is presented in Appendices A and B, respectively. It should be mentioned that to date it is still a big challenge to accurately separate different phases based on XCT images, due to the limited resolution. Nevertheless, the relative change of microstructure of a specific area, e.g., fly ash and slag particles at different curing ages can be estimated using the same segmentation method, which is the primary focus of this study.

After segmentation, the identified phases were labelled as different connected clusters to characterise the morphological features, e.g., surface area and volume, considering the voxel connectivity. Three types of voxel connectivity (6-, 18- and 26-connectivity) are commonly used to analyse the morphological structure. The voxels share the same face are considered as connected in the type of 6-connectivity, while the 18-connectivity represents the connected voxels with a common edge. Regarding 26-connectivity, the voxels that share the same vertex are regarded to be connected. Here, the type of 26-connectivity is used to obtain accurate results.

Finally, the labelled clusters extracted from the image were quantified based on the voxel number of the labelled region and the voxel size of the image. For example, the volume of the labelled region can be calculated as:

$$V = N_v \times S_v \quad (1)$$

where V represents the volume of the labelled area (μm^3), N_v denotes the number of voxels (-), and S_v is the spatial resolution (voxel size) of the image (μm^3).

4. Results and discussion

4.1. Microstructure evolution of fly ash particle in AAFS

4.1.1. Phase identification

Fig. 3 shows the local histogram of grey value of fly ash particle, which can be used to identify

different phases in this particle. The red line across the fly ash particle from point A to point E indicates the location of grey value (Fig. 3a). The linear grey value against distance from the core position of fly ash particle is illustrated in Fig. 3b, where the grey value stays at the highest value of 255 between points A and B (located between 0 μm and 1.66 μm), representing the unreacted fly ash particle with the highest density among the phases in this local area. With the increase of distance from 1.66 μm to 30 μm (B – D), the grey value decreases sharply from 255 to 100, suggesting the presence of reaction products with various densities. The grey value at around 100 between point D and point E (located between 30 μm and 40 μm) corresponds to the area of paste matrix with the lowest density. The area of reaction products (B – D) can be further divided into inner products and outer products, based on their difference in grey value and their locations relative to the original boundary of fly ash particle. The linear area of inner products (B –C) covers the grey values between 178 and 255, while the linear area of outer products (C – D) belongs to the grey values between 100 and 178. The inner products with a relatively high grey value indicate that the density of inner products is higher than that of outer products. Also, a polychromatic image is used to visualize the distribution of different phases of fly ash particle. As seen in Fig. 3c, the unreacted fly ash is labelled as yellow, while the inner products and outer products are labelled as red and green, respectively. The paste matrix is labelled as white.

It can be observed that there is a gradual transition of grey value at the boundary between unreacted particle and reaction products, as schematically illustrated in Fig. 3d. It is the result of overlapping of these two phases at the boundary due to the limited resolution of XCT image, i.e. 1.56 μm, which is higher than the size of the elementary components of reaction product (gel matrix) with a length scale of 10 nm ~ 1 μm [49] and thus the pixels at the boundary between particle and reaction products would tend to cover the grey values of both two phases. The gradual transition of grey value at the boundary is a common phenomenon existing in XCT imaging [26, 50], which would bring uncertainty regarding the selection of true boundary of phases. The threshold value for reaction products may be either the upper, middle or lower end of the transition zone and accordingly the measured reaction products would be different. It has been demonstrated that a closer estimation of the threshold value can be obtained if selecting the grey value at the upper end of the transition region [51]. Therefore, in this study, the grey value at the upper end of transition region is used to determine the boundary between unreacted particle and reaction products. Here, it is worth mentioning that the accuracy of XCT image is lower than that of BSEM image due to its relatively lower resolution. Generally, the pixel size of XCT image can reach microscale, while the optimal pixel size of BSEM image can be adjusted to nanoscale [52, 53]. However, it has been demonstrated that the results of phases identification and quantification based on XCT image agree well with that obtained from BSEM image [54]. In addition, as the pixel size of XCT image in this

study is 1.56 μm that is smaller than the thickness of reaction products around fly ash and slag particles with a range of several microns, the magnification of XCT image can still fulfil the requirement of phases identification and quantification using grey level histograms. Thus, the XCT image can provide reliable information for the in-situ monitoring of reaction process of fly ash and slag particles in AAFS system.

Fig. 4 shows the chemical composition of fly ash particle characterised using BSEM-EDS, where the BSEM-EDS line analysis encompassing core particle-paste matrix is displayed in Fig. 4a. There exists a slightly high grey value at the boundary of particle due to the charging effect of BSEM tests. The charging effect arising from electron/ion irradiation is unavoidable when a non-conductive specimen is tested using BSEM [55]. The molar ratios of Ca/Si, Ca/Al and Ca/(Si+Al) along the distance from the core of fly ash particle are plotted in Fig. 4b. These element ratios of the original fly ash particle are also provided to better separate the unreacted region and the reacted region of particle. Based on the chemical composition of fly ash particle (Table 1), the Ca/Si, Ca/Al and Ca/(Si+Al) molar ratios of original fly ash particle are calculated as 0.04, 0.07 and 0.026, respectively.

It should be noted that it is challenging to make a comparison of the element ratios for the same particle over time based on BSEM-EDS test, as it is a destructive testing method and the sample needs to be cut, grinded, dried and polished. It can be found that the Ca/Si ratio stays at a low level (< 0.05) in the core region of particle (A – B), which is close to the Ca/Si ratio existed in the original fly ash particle (0.04). Such low Ca/Si ratio can be ascribed to the low content of Ca in the fly ash particle. The Ca/Si ratio is then increased rapidly from 0.1 to 0.45 in the inner region within the boundary of particle (B – C), attributing to the supply of Ca ions from the dissolution of outside particles, e.g., slag particles. The Ca/Si ratio becomes stable at a constant level between 0.4 and 0.5 in the outer region of particle (C – D) and the paste matrix (D – E) due to the relatively uniform distribution of Ca and Si ions. Similar trends can be observed in the distribution of Ca/Al and Ca/(Si+Al) ratios, suggesting the diffusion of ions from bulk solution into the fly ash particle, which would lead to the dissolution of particle and the formation of reaction products.

4.1.2. Reaction depth and reaction degree characterisation

Fig. 5 shows the 3D internal structure of fly ash particle, which can be used to characterise the interior changes of particle structure. It can be seen from Fig. 5a that the morphology of fly ash particle is modified along with the formation of reaction products. Here, the central slice of the fly ash particle is selected as the typical slice to quantify the interior changes of particle, i.e., reaction depth (Fig. 5b). The reaction depth of fly ash particle is quantified by the distance between the boundary of outer products and the boundary of unreacted fly ash. The unreacted area labelled as yellow gives the boundary of unreacted fly ash (see the black dash circle). The grey dash circle

denotes the boundary of inner products, while the black solid cycle stands for the boundary of outer products. Fig. 5c shows the reaction depths in the horizontal and vertical directions, which can be measured based on the difference of grey value in the linear local histogram of grey value. Accordingly, the reaction depths in horizontal and vertical directions are quantified as: D_1 = 11.37 μm, D_2 = 7.12 μm, D_3 = 7.21 μm, and D_4 = 6.68 μm. The reaction degree of fly ash can be calculated based on the volume change of fly ash particle as follows:

$$\alpha_{FA}=\left(1-\frac{V_{(t)FA}}{V_{(0)FA}}\right)\times 100\% \quad (2)$$

where α_{FA} is the reaction degree of fly ash particle, $V_{(t)FA}$ is the volume of unreacted fly ash at curing age *t*, and $V_{(0)FA}$ is the initial volume of fly ash particle before reaction.

It should be mentioned that it is unlikely to obtain the "real" initial volume of fly ash particle due to the long testing time (~ 7 h). Nevertheless, since the formation of inner products is within the boundary of the original particle, the volume within the boundary of inner products can be assumed as the initial volume of fly ash particle. Accordingly, $V_{(0)FA}$ can be calculated based on the volume within the boundary of inner products in the fly ash particle at 1 d. Therefore, the relative volume change (i.e., reaction degree) of the same fly ash particle at different curing ages can be obtained and compared. The reaction rate of fly ash particle at different curing stages can be calculated as:

$$R_{FA}=\frac{\alpha_{(i+1)FA}-\alpha_{(i)FA}}{t_{(i+1)}-t_{(i)}} \quad (3)$$

where R_{FA} is the reaction rate of fly ash particle, $\alpha_{(i)FA}$ is the reaction degree of fly ash at stage *i*, $\alpha_{(i+1)FA}$ is the reaction degree of fly ash at stage i+1, $t_{(i)}$ is the curing age at stage *i*, and $t_{(i+1)}$ is the curing age at stage i+1.

There are four curing stages, including stage 1 at 1 d, stage 2 at 3 d, stage 3 at 7 d, and stage 4 at 28 d corresponding to four curing ages, i.e., 1, 3, 7, and 28 d.

4.1.3. Microstructure evolution with curing age

Fig. 6 illustrates the greyscale image of fly ash particle and its linear grey value histogram at different curing ages. The different morphology and grey values observed for different phases (e.g., unreacted fly ash and reaction products) allow us to explore how the fly ash particle is dissolved and how the reaction products are involved in its dissolution process. In the first image scanned at 1 d, rounded fly ash particle is visible in white, surrounded by a layer of reaction products in light grey and the paste matrix in dark grey. The grey value histogram highlights the presence of unreacted fly ash located between 38.42 μm and 77.73 μm (with the highest grey value of 255), surrounded by the reaction products with grey values of around 100 – 255. From1 d to 28 d, the area of unreacted fly ash is decreased steadily, while the area of reaction products is increased (see greyscale image in Fig. 6). This indicates that the fly ash particle is dissolved under the activation of

alkaline activator along with the formation of reaction products. It is confirmed by the decrease of the grey value in the initial location of unreacted fly ash, as seen the grey value histogram in Fig. 6. It is interesting to note that the dissolution of fly ash mainly results in the formation of inner products, indicating that most changes of fly ash microstructure are interior where the original boundary of fly ash is maintained during the dissolution process.

As seen in Fig. 7, the reaction depth and reaction degree of fly ash particle at different curing ages are quantified to further understand its microstructural evolution. The 3D microstructure evolution of fly ash particle is presented in Fig. 7a. At 1 d, the fly ash particle changes within its original boundary along with the formation of inner products, but fewer outer products are formed outside its original boundary. This indicates that most ions from the dissolution of fly ash cannot diffuse into the surrounding regions, but are trapped inside the boundary of original particle, leading to the formation of inner products at this early age. Between 3 d and 28 d, more areas of fly ash particle are changed along with the precipitation of more inner products. In the meantime, more outer products are formed outside the boundary of fly ash particle, especially at 7 d and 28 d, which suggests that more dissolved ions have transported from the dissolution of fly ash particle to the outer region of particle, resulting in the precipitation of outer products. In addition, it can be observed that the dissolution of fly ash particle is not uniform, where the particle dissolution along the X-direction is more obvious than that in Y- and Z-directions at 28 d.

To further characterise the microstructure evolution of fly ash particle, three central slices in different directions (i.e. X-Y, X-Z and Y-Z) are used to estimate its reaction depth, where eight directions from direction a to direction h in each slice are quantified, as shown in Fig. 7b-d, the results of which are demonstrated in Fig. 7e. Regarding the X-Y central slice, the reaction depths in all directions are close to each other at the beginning (1 d), except for the reaction depth in direction g. The reaction depth indirection g is 11.37 μm higher than that in other directions (4.94 – 7.23 μm), implying the area in direction g is preferentially reacted in comparison with other areas. From 1 d to 3 d, the reaction depths in all directions are increased, especially for the reaction depths in directions c, d and e. At 3 d, the reaction depths in directions c, d and e are increased significantly from 6.89 μm, 4.93 μm and 6.66 μm to 9.19 μm, 12.17 μm and 10.11 μm, respectively. This suggests that the reaction levels at the bottom right area (from direction c to direction e) are higher than other areas during these curing ages. As the reaction continues from 3 d to 28 d, the reaction depths at the bottom right area are continuously increased, while the reaction depths at other areas are also increased steadily. At 28 d, it can be observed that the reaction depths in directions c, d, e and g are higher than those in other directions. Similar trends can also be found in the X-Z and Y-Z central slices, where the reaction depths in some areas are higher than others. This implies that the dissolution behaviour of fly ash particles presents some homogeneity at early ages but becomes

non-uniform at later curing ages.

Fig. 7f shows the reaction degree and reaction rate of fly ash at different curing ages. The reaction degree of fly ash is increased slowly from 15.81% to 19.07% at the early ages between 1 d and 3 d. It is then increased dramatically from 19.07% to 33.80% at 7 d, and finally increases to 57.67% at 28 d. This agrees well with the findings reported in [49, 56] that the reaction degree of fly ash at 28 d can get a level in the range of 46% and 75% with appropriate alkaline activators. By contrast, it can be seen from Fig. 7f that the reaction rate of fly ash is reduced dramatically from 15.81%/d to 1.63%/d between the first curing stage (0 – 1 d) and the second curing stage (1 – 3 d). And then, it is increased slightly to 3.68%/d at the third stage (3 – 7 d) and finally decreased to 1.14%/d at the last stage (7 – 28 d). This phenomenon can be attributed to the formation of inner products at 1 d, which would physically block the unreacted fly ash particle and the outside solution and thus reduce the transportation of dissolved ions, leading to the decrease of dissolving rate of fly ash particle and consequently the reaction rate [57].

4.1.4. Effect of particle structure

It is known that fly ash particles have two main structures, including the solid structure and the hollow structure. Thus, it is necessary to evaluate the effects of particle structure on the microstructure evolution of fly ash. The solid and hollow fly ash particles with a similar size were chosen to estimate these effects. Fig. 8 displays the 3D structures and 2D slices of solid and hollow fly ash particles. The solid fly ash particle is found to be spherical and unbroken, while the hollow fly ash particle has a largely empty hollow core. In addition, the shape of the solid fly ash particle is more regular compared to the hollow fly ash particle. The greyscale slice and the linear grey value histogram of hollow fly ash are presented in Fig. 9 to characterise its microstructure evolution. It can be observed that the reaction products formed during the reaction of hollow fly ash not only accumulate around the outer surface of particle but also accumulate inside the particle due to the presence of hollow core. This indicates that the fly ash particle with a hollow structure would be activated simultaneously from the outside in and from the inside out, leading to the accelerated reaction process. The overall area of hollow fly ash particle is dissolved faster than that of solid fly ash particle, especially for the left side area which is fully reacted at 28 d. This phenomenon is confirmed by the relatively high reaction degree of fly ash particle with a hollow structure compared to that of solid fly ash particle, regardless of curing age (Fig. 10a). Here, the reaction degrees of hollow fly ash at 1, 3, 7 and 28 d are found to 28.15%, 32.05%, 44.71% and 64.92%, respectively, which are higher than that of solid fly ash at the same curing ages, i.e., 15.81%, 19.07%, 33.8% and 57.67% at 1, 3, 7 and 28 d, respectively. As seen in Fig. 10b, the changing trend of reaction rate of hollow fly ash particle is similar to that of solid fly ash particle, both of which are gradually decreased with the increase of curing age.

4.1.5. Effect of particle size

The particle size of the initial fly ash particle would influence its microstructure evolution. To evaluate such effect, five fly ash particles with different diameters ranging from about 50 μm to 10 μm are chosen and the evolution of their microstructures is investigated. The selection of the typical size of fly ash particle is based on the particle size distribution, where the size of 90% fly ash is smaller than 32.86 μm and 50% fly ash has a size larger than 10 μm (Table 2). In addition, the limitation of the XCT image resolution (1.56 μm) would also affect the selection of fly ash particle. Here, the size of fly ash particle is measured as the spherical equivalent diameter (d_{Eq}) that is calculated based on the volume of fly ash particle. The obtained d_{eq} of these five fly ash particles from particle 1 to particle 5 are 56.59 μm, 41.30 μm, 28.14 μm, 16.63 μm and 12.93 μm, respectively.

Fig. 11 shows the microstructure evolution of five fly ash particles (particle 1 to particle 5). The central slice of each particle is used to characterise the development of reaction depths, in which eight directions (from direction a to direction h) are quantified as illustrated in Fig. 11a and b. At 1 d, the reaction depths in all directions of each particle are close to each other, except that in the direction g in particle 1, which indicates that most particles are activated uniformly around the spherical fly ash particle at 1 d. At this stage, the order of average reaction depth for different particles is particle 1 > particle 3 > particle 4 > particle 2 > particle 5, which is different with the order of particle size from particle 1 to particle 5, implying that there is no obvious positive relationship between the particle size and reaction depth of fly ash particle. At 3 d, the reaction depths in different directions for all particles are increased, but at different levels. For particles 1, 2 and 3, the reaction depths in some directions are higher than that in other directions, i.e., directions c, d, e and g in particle 1, direction h in particle 2, and directions f, g and h in particle 3. However, the reaction depths in all directions are still close to each other in particles 4 and 5. With the increase of curing age from 3 d to 28 d, the discrepancy of reaction depths in different directions in particles 1, 2 and 3 becomes more obvious, while the reaction of particles 4 and 5 is still uniform. This indicates that the reaction of fly ash particle with a relatively large size is easier to become asymmetrical than that of the particle with a smaller size.

It can be seen from Fig. 11c that the reaction degrees of all particles are increased steadily with the increase of curing age, which generally follow an order of particle 1 < particle 2 < particle 3 < particle 4 < particle 5. This suggests that the fly ash particle with a smaller size would be easier activated due to its relatively high specific area. As seen in Fig. 11a, the fly ash particle with the smallest size (particle 5) is fully reacted at 28 d, while the reaction degree of particle 2 (45.64%) is lower than that of particle 1 (57.67%) at 28 d, which can be ascribed to the heterogeneous characteristics between these two particles, where particle 2 may have a relatively high content of

crystal phases, resulting in a relatively low reaction degree. Moreover, the reaction rates of all particles are decreased dramatically after 1 d, which implies that the formation of inner products would indeed prevent the contact between unreacted fly ash and alkaline solution and inhibit the further reaction of fly ash particle, regardless of its size.

4.1.6. Mechanism of microstructure evolution

The microstructure evolution of fly ash particle can be divided into two parts: the dissolution of particle and the formation of reaction products, as shown in Fig. 12. It can be seen from Fig. 12a that the fly ash particle is dissolved upon the activation of alkaline activator (SS and SH) via rupture the Si-O-Si and Al-O-Al bonds in fly ash. An irregular shape can be observed in the reacted fly ash particle, indicating that the reaction of fly ash is not uniform, which varies from point to point on the surface. It can be attributed to the inherently heterogeneous characteristics of fly ash particle that consists of relatively inert crystal phases and highly reactive amorphous phases [58]. This suggests that the area of fly ash particle with a high proportion of amorphous phases could be easier activated, resulting in a rapid localized dissolution.

Once the fly ash particle is dissolved, a variety of dissolved species are generated, including silica monomers (e.g. $Si(OH)_4$) and alumina monomers (e.g. $Al(OH)_4^-$)). With the increase of monomer species, the monomers would react with each other to form dimers such as silica dimers and silica-alumina dimers. Afterwards, the reaction products start to form and precipitate in the dissolved area of fly ash particle. The reaction products can be typically classified as inner products and outer products, according to the location relative to the original boundary of fly ash particle and the difference in density and composition, as discussed in Section 4.1.1. It can be seen from Fig. 12b that the reaction products region is asymmetrically distributed around the unreacted fly ash particle, due to the inhomogeneous dissolution of fly ash particle.

Besides, most reaction products accumulate within the boundary of the original particle, suggesting the formation of inner products as a result of the reaction process of fly ash. Once the region of fly ash particle reacts with the solution, etch pits start to form on the surface, leading to the locally rapid dissolution inside the pits. This rapid dissolution would greatly increase the ionic concentration inside the pits, which would make the supersaturation in these pit areas and promote the nucleation of reaction products. Afterwards, the nuclei of reaction products would start to grow and fill the pits, until they reach the original surface of particle. And then, the growth would become slow when the reaction products reach the boundary of original particle due to the relatively low ionic concentration in the surrounding regions.

Furthermore, as seen in Fig. 12b, the early formation of inner products would naturally build a physical barrier between the unreacted particle and the outside solution, which would prohibit the diffusion of ions from bulk solution to the core particle [57]. Consequently, the diffusion of ions

from bulk solution to the unreacted particle would become difficult as the ions need to penetrate through the porous reaction products (e.g. N-A-S-H gels [59]) or the microcracks in the precipitation layer instead of the direct contact with the unreacted particle [60]. The formation of microcracks in the precipitation layer can be ascribed to the nonuniform reaction on the surface of particle, which leads to the variation of products precipitation from one surface location to another. Accordingly, the diffusion rate of ions from bulk solution to the unreacted particle would be decreased, and consequently slow down the reaction process of fly ash. It is confirmed by the significant decrease of reaction rate of fly ash particle after 1 d, regardless of particle shape and particle size (Fig. 10b and 11d), and agrees well with the descriptive model presented in previous research [15].

4.2.Microstructure evolution of slag particle in AAFS

4.2.1. Phase identification and characteristics

Fig. 13 shows the linear grey value against distance from the core position of slag, based on which different phases in slag particle can be identified. As seen in Fig. 13a and b, the grey value of unreacted slag is measured to be 160 between point A and point B (located between 0 μm and 10.58 μm). The location between 10.58 μm and 26.20 μm (B – C) represents the region of inner products, covering the grey values of 132 – 160. The outer products (C – D) have grey values of 94 – 132, while the paste matrix (D – E) covers the grey values around 94. Accordingly, the different phases in slag particle can be labelled as different colours in Fig. 13c, where unreacted slag, inner products, outer products, and paste matrix are displayed in yellow, red, green, and white, respectively.

Fig. 14 illustrates the chemical composition of slag particle characterised using the BSEM-EDS line scanning from the core position of slag to the paste matrix. The molar ratios of Ca/Si, Ca/Al and Ca/(Si+Al) against the distance from the core position of slag are quantified and presented in Fig. 14a and b. In addition, these element ratios of the original slag particle are also obtained based on its chemical composition (Table 1), where the molar ratios of Ca/Si, Ca/Al and Ca/(Si+Al) are found to be 1.34, 2.85 and 0.91, respectively. The Ca/Al ratio stays at a high level (> 1.8) at the core region of particle (A – B), consisting with the high Ca/Al ratio in the original slag particle, which can be ascribed to the high content of Ca in the slag particle. The Ca/Al ratio is decreased significantly from 1.8 to 0.6 in the inner region of particle (B – C), which can be attributed to the supply of Al ions from the dissolution of outside particles, e.g., fly ash particles. The Ca/Al becomes stable between 0.6 and 0.8 in the outer region of particle (C – D) and the paste matrix (D – E), due to the relatively uniform distribution of Ca and Al ions. Similar trends can be observed in the distribution of Ca/Si and Ca/(Si+Al) ratios. The diffusion of ions into the slag particle indicates that the slag would be dissolved under the activation of bulk solution, leading to the formation of reaction products.

The estimations of reaction depth and reaction degree slag follow a similar approach for fly ash as mentioned in Section 4.1.2. The distance between the boundary of the outer products and the boundary of the unreacted slag is regarded as the reaction depth. The reaction degree of slag can be calculated based on the volume change of the slag particle as follows:

$$\alpha_{slag}=\left(1-\frac{V_{(t)slag}}{V_{(0)slag}}\right)\times 100\% \quad (4)$$

where α_{slag} is the reaction degree of fly ash particle, $V_{(t)slag}$ is the volume of unreacted fly ash at curing age t, and $V_{(0)slag}$ is the initial volume of fly ash particle calculated from the volume within the boundary of inner products at 1 d.

The reaction rate of slag particle at different curing stages can be calculated as:

$$R_{slag}=\frac{\alpha_{(i+1)slag}-\alpha_{(i)slag}}{t_{(i+1)}-t_{(i)}} \quad (5)$$

where R_{slag} is the reaction rate of fly ash particle, $\alpha_{(i)slag}$ is the reaction degree of fly ash at stage i, $\alpha_{(i+1)slag}$ is the reaction degree of fly ash at stage i+1, $t_{(i)}$ is the curing age at stage i and $t_{(i+1)}$ is the curing age at stage i+1.

Similarly, four curing stages including stage 1 at 1 d, stage 2 at 3 d, stage 3 at 7 d and stage 4 at 28 d corresponding to four curing ages of 1, 3, 7 and 28 d, respectively are considered for further analysis.

4.2.2. Microstructure evolution with curing age

As seen in Fig. 15, the microstructure evolution of slag particle is characterised with the assistant of the greyscale image and its linear grey-value histogram. At 1 d, the unreacted slag covers a relatively wide area located between 17.58 μm and 42.40 μm, surrounded by a thin layer of reaction products. Between 3 d and 28 d, the region of unreacted slag is reduced steadily, while the region of reaction products is increased, confirmed by the grey value histogram, which suggests the dissolution of slag particle and the formation of reaction products under the activation of alkaline activator.

Fig. 16 shows the internal microstructural changes of slag particle with increasing curing ages. It can be seen from Fig. 16a that the slag particle is heterogeneously varied and covered by the reaction products, where the reactions of some regions are more extensive than others at 1 d. The 3D inner structure indicates that most regions of slag particle evolve within its original boundary along with the formation of inner products and fewer products can be observed outside its original boundary (i.e., the formation of outer products). It implies that the dissolved region of slag accumulates a higher concentration of ions compared to the surrounding regions, which would result in a rapid reaction and promote the formation of reaction products in this region (i.e., inner products). From 3 d to 28 d, the slag particle is continually reacted accompanied by the formation of

more inner products. In addition, more outer products are also found at later curing ages (7 d and 28 d), attributing to the transport of more dissolved ions from inner region to outer region of slag particle.

The microstructure evolution of slag particle along different directions (i.e., X-Y, X-Z and Y-Z) at three central slices is shown in Fig. 16b-d, respectively. The reaction depths of these slices in eight directions from direction a to direction h are quantified and presented in Fig. 16e. For the X-Y central slice, the reaction depth in direction f is higher than that in other directions at 1 d. The reaction depth in direction f is 17.24 μm, while the reaction depths in other directions are in the range of 4.37 – 8.44 μm. It is indicated that the reaction of slag particle is not uniform, and the area in direction f is preferentially activated. As the curing age increases from 3 d to 28 d, the heterogeneous reaction of slag particle proceeds, which leads to the relatively high reaction depths in directions a, f and h at 28 d. Similar developing trend of reaction depth can also be observed in the X-Z and Y-Z central slices, suggesting that some areas of slag particle are preferentially activated than other areas.

The reaction degree and reaction rate of slag particle at different curing ages are quantified and shown in Fig. 16f. It can be found that the reaction degree of slag is increased steadily from 25.19% to 61.31% between 1 d and 28 d. This is consistent with the result reported in literature that the reaction degree of slag at 28 d can reach around 60% [61, 62]. Nevertheless, its reaction rate is decreased dramatically from 25.19%/d to 6.63%/d between first curing stage (0 – 1 d) and second curing stage (1 – 3 d), followed by a continuous reduction to 0.59%/d at the last stage (7 – 28 d), which suggests that the early formation of inner products at 1 d would influence the reaction rate at later curing ages. Once the inner products are formed on the surface of slag particle, they would physically block the unreacted slag and the surround solution, leading to a reduction of the further dissolution of slag.

4.2.3. Effect of particle size

To estimate the effect of particle size on microstructure evolution of slag particle in AAFS, five slag particles with a diameter ranging from about 75 μm to 10 μm are selected, which mostly covers the particle size distribution of slag used in this study (Table 2). The size of slag particle is referred to as the maximum diameter (d_{max}) that is measured as the maximum distance between two points in the original boundary of the central slice in X-Y direction. The d_{max} values of the five slag particles from particle 1 to particle 5 are found to be 74.76 μm, 64.22 μm, 36.04 μm, 21.42 μm and 9.48 μm, respectively.

Fig. 17 shows the microstructure evolution of five slag particles (particle 1 to particle 5) at different curing ages. The reaction depths of different particles at eight directions are quantified and illustrated in Fig. 17a and b. The average reaction depths for different particles follow an order of

particle 1 > particle 2 > particle 3 > particle 4 > particle 5, which is consistent with the order of particle size from particles 1 to 5. This implies that the size of slag particle has a positive influence on its reaction depth. At the beginning (1 d), there exists a close reaction depth at all directions in each particle, except for the direction f in particle 1, which suggests that most particles are activated uniformly around the slag particle at 1 d. At 3 d, the reaction depths at different directions for all slag particles are increased, but at different levels. The reaction depths in direction f in particle 1 and direction g in particle 2 are higher than those at other directions, while the reaction depths at all directions are still close to each other in particles 3, 4 and 5. At 7 d, the heterogeneous reaction can also be observed in particles 3 and 4, where the reaction depths in some directions are higher than those in other directions, e.g., the directions a, b and c in particle 3 and direction a in particle 4. With the increase of curing age from 7 d to 28 d, the discrepancy of reaction depths in different directions in particles 1, 2 and 3 becomes more obvious, while the reaction of particles 4 and 5 is uniform. This implies that the slag particle with a relatively large size tends to experience a non-uniform reaction compared to that with a smaller size.

The reaction degrees and reaction rates of all slag particles are quantified and shown in Fig. 17c and d. As seen in Fig. 17c, the reaction degrees of all slag particles are increased steadily with the increase of curing age. At 1 d, it can be found that the slag particles with a smaller size have a higher reaction degree, where the reaction degree follows an order of particle 5 (70.91%) > particle 4 (49.74%) > particle 3 (41.88%) > particle 2 (27.44%) > particle 1 (25.19%). This indicates that the size of slag particle would indeed significantly affect its chemical reaction and microstructural evolution in AAFS. The slag particles with smaller size would be activated more easily due to the relatively high specific area. However, the reaction degree of particle 2 (29.66%) becomes smaller than that of particle 1 (38.46%) at 3 d, which implies that the reaction of slag particle may also be affected by other factors, such as the morphology and chemical composition of slag. With the increase of curing age from 3 d to 28 d, the difference of reaction degree between the small slag particle (particle 4 and particle 5) and the large slag particle (particles 1, 2 and 3) becomes more obvious. Particle 5 and particle 4 are fully reacted at 7 d and 28 d, respectively, while the other particles share a similar reaction degree of about 60% at 28 d. As seen in Fig. 17d that the reaction rates of all slag particles are reduced significantly after 1 d, which suggests that the initially formed inner products would indeed prevent the further reaction of slag particle, regardless of its size.

4.2.4. Mechanism of microstructure evolution

Fig. 18 shows the microstructural changes of slag particle with curing ages, in terms of the dissolution of particle and the formation of reaction products. At the beginning, the diffusion of alkaline solution into the slag particle would rupture the Ca-O and Si-O-Si bonds in slag, thereby dissolving the slag particle and reducing its size. It can be seen from Fig. 18a that the original slag

particle is dissolved and an irregular sharp of the unreacted particle is formed due to the non-uniform dissolution. Some regions of the slag particle experience more dissolution than others, which can be attributed to the heterogeneous distribution of chemical composition of slag and the initial defects induced by the mechanical damage during the grounding process of AAFS sample. These special regions would promote the formation of etch pits and result in the rapid localized dissolution. A similar phenomenon can also be observed in the dissolution of fly ash particle in AAFS mixes as discussed in Section 4.1.6.

After the dissolution of slag particle, a thin layer of reaction products is formed around the unreacted slag particle, as shown in Fig. 18b. It can be found that the distribution of reaction products is not uniform around the slag surface, attributing to the non-uniform dissolution of slag. The reaction products can be divided into inner products and outer products. The proportion of inner products is higher than that of outer products, as a result of the rapid reaction in the dissolved region of slag, where the high ionic concentration would promote the formation of reaction products, filling the dissolved region. When the dissolved region of slag is filled with the inner products, the growth of reaction products would drop due to the relatively low ionic concentration surrounding the outside particle. Besides, it can be seen from Fig. 18b that the formation of inner products (e.g. C-A-S-H gels [63]) would also act as a physical barrier, preventing the diffusion of ions between unreacted slag and the surrounding region and thus slowing down the reaction process. It is responsible for the sharp decrease of reaction rate of slag particle after 1 d, regardless of particle size (Fig. 17). A similar phenomenon can be found in the formation of reaction products of fly ash particle in AAFS as mentioned above.

4.3.Interaction between fly ash and slag particles in AAFS

4.3.1. Phase identification

Fig. 19 demonstrates the linear grey value across the adjacent slag and fly ash particles. The unreacted slag with a grey value of 230 (C – D) and unreacted fly ash with a grey value of 255 (G – H) are surrounded by the reaction products and paste matrix. The reaction products of slag (B – C; D – E) cover the grey values of 120 –230, while the reaction products of fly ash (F – G; H – I) correspond to the grey values of 108 – 255. The reaction products of slag and fly ash can also be divided into inner and outer products based on their difference in grey value and their relative locations to the original boundary of particle, as mentioned in Sections 4.1.1 and 4.2.1. Similarly, different phases in slag and fly ash particles are also labelled as different colours (unreacted particle: yellow; inner products: red; outer products: green; paste matrix: white).

Fig. 20 shows the chemical composition across slag and fly ash particles characterised by means of the BSEM-EDS line scanning from slag to fly ash. The molar ratios of Ca/Si, Ca/Al and Ca/(Si+Al) against the distance from slag to fly ash are calculated and plotted in Fig. 20a and b. The

Ca/Al ratio stays at a relatively high level (> 1.0) at the core region of slag (A – B) and reduces from 1.0 to 0.43 at the outer region of slag (B – C), followed by a further slight reduction from 0.43 to 0.26 in the region of paste matrix between slag and fly ash (C – D). The Ca/Al ratio drops from 0.26 to 0.03 in the outer region of fly ash (D – E) but becomes stable at around 0.03 in the core region of fly ash (E – F). The continuous decrease of Ca/Al ratio from the region of unreacted slag fly ash can be attributed to the decline of Ca content and the increase of Al content due to the ion transport during the dissolution of slag and fly ash. The Ca dissolved from slag particle would diffuse to the region close to fly ash particle due to the gradient of ionic concentration. Similarly, the dissolution of Al from fly ash would also diffuse to the slag region. Similar trends can be observed in the distribution of Ca/Siand Ca/(Si+Al) ratios.

4.3.2. Interaction of fly ash and slag at various curing ages

Fig. 21 displays the interaction between fly ash and slag particles at different curing ages, characterised using the greyscale image and the linear grey value histogram. At the beginning (1 d), both unreacted slag and fly ash particles occupy a relatively wide area, surrounded by a thin layer of reaction products. At 3 d, the areas of unreacted slag and fly ash are both slightly reduced, while the areas of reaction products of slag and fly ash are increased accordingly. However, the microstructure evolution of slag and fly ash becomes different after 3 d. Between 7 d and 28 d, the area of unreacted slag is reduced steadily, following a similar changing trend observed in the isolated slag, as discussed in Section 4.2.2. This indicates that the presence of fly ash has a slight effect on the microstructure evolution of slag. Nevertheless, the area of unreacted fly ash is reduced significantly between 7 d and 28 d. At 7 d, fly ash particle is dissolved quickly, leading to an irregular shape of unreacted fly ash, as confirmed by the obvious decrease of grey value. At 28 d, the fly ash particle is completely dissolved, resulting in a fully reacted area with reaction products.

The reaction degree and reaction rate of slag and fly ash at different curing ages are quantified and presented in Fig. 22 to further understand the interaction between slag and fly ash particles in AAFS. As seen in Fig. 22a, the microstructure evolution of slag particle close to fly ash particle is similar to that of isolated slag particle (Fig. 16a), where the slag particle is dissolved steadily accompanied by the formation of inner products. Nevertheless, the microstructure evolution of fly ash particle close to slag particle is different compared to the isolated fly ash particle (Fig. 7a). The original boundary of fly ash disappears after 7 d along with the formation of outer products in paste matrix, which can be attributed to the accelerated reaction of fly ash particle. It can be seen from Fig. 22b that the reaction degree of slag is increased steadily from 36.28% to 62.89% between 1 d and 28 d, following a similar changing trend of isolated slag (Fig. 16f), while the change of reaction degree of fly ash is different from that of isolated fly ash, which is increased steadily with increasing curing age from 1 d to 28 d (Fig. 7f). Here, the reaction degree of fly ash is increased

slightly from 22.56% to 28.80% with the increase of curing age from 1 d to 3 d, but then increased significantly to 72.50% at 7 d and eventually reaches 100% at 28 d. Besides, it can be found that the reaction degree of slag (36.28% – 47.05%) is higher than that of fly ash (22.56% – 28.80%) at early ages (1 – 3 d). Afterwards, the reaction degree of slag (53.50% – 62.89%) becomes lower than that of fly ash (72.50% – 100%) between 7 d and 28 d. Furthermore, it can be seen from Fig. 22c that the change of reaction rate of slag near the fly ash particle in AAFS is similar to that of isolated slag (Fig. 16f), where the reaction rate reduces from 36.28%/d to 5.39%/d during the first curing stage (0 – 1 d) and the second curing stage (1 – 3 d) and continually drops to 0.45%/d at the last stage (7 – 28 d). However, the changing trend of reaction rate of fly ash near the slag particle in AAFS is different from that of isolated fly ash (Fig. 7f). The reaction rate of fly ash is decreased significantly from 22.56%/d to 3.12%/d during the first and second stages, followed by a sharp increase to 10.92%/d at the third stage (3 – 7 d) and a sharp decrease to 1.30%/d at the last stage (7 – 28 d).

It is indicated that the presence of slag would strongly accelerate the chemical reaction and microstructure evolution of fly ash in AAFS, which is completely different from the microstructure evolution of isolated fly ash, as discussed in Section 4.1.3. To further verify this phenomenon, the dissolution behaviour of fly ash particles near slag particles at three different locations was estimated, as shown in Fig. 23. It can be observed that the presence of slag particles would indeed accelerate and promote the reaction process of fly ash particles, leading to a relatively high reaction degree of fly ash particles, ranging from 66% to 84%. The variation of reaction degree of fly ash particles can be attributed to the difference of particle size, chemical composition, and initial defects in different particles.

4.3.3. Mechanism of interaction between fly ash and slag

The interaction between fly ash and slag in AAFS can be associated with their different reaction mechanisms. During the alkaline activation, different types of chemical elements would be dissolved from fly ash and slag particles, leading to the formation of different reaction products [18]. The Si and Al ions would be dissolved from fly ash to form N-A-S-H gels, while the Ca, Si and Al ions would be dissolved from slag to form C-A-S-H gels. Therefore, it is likely to occur interaction and reaction of dissolved ions, which would further affect the surrounding aqueous environment of fly ash and slag, resulting in the interaction between them in terms of microstructure evolution [16].

As shown in Fig. 22, the microstructure evolution of fly ash and slag at early ages (1 – 3 d) is similar to that of isolated fly ash (Fig. 12) and slag (Fig. 18), respectively, which indicates that the interaction between fly ash and slag is not obvious at early ages. This can be ascribed to the limited movement of the dissolved ions between fly ash and slag particles. At these early ages, the reaction degree of fly ash is smaller than that of slag due to its relatively low reactivity. At later curing ages (7 – 28 d), the trend of microstructure evolution of fly ash becomes different from that of slag. The

microstructure of fly ash exhibits a significant change with the increase of curing age from 7 d to 28 d, indicating the existence of interaction between fly ash and slag. This can be attributed to the diffusion of Ca ions from the dissolved slag to the unreacted fly ash, which would enhance the rate and the extent of fly ash dissolution and the formation of reaction products [16]. The presence of Ca ions would facilitate and promote the precipitation of Ca-based products (C-A-S-H gels), which would act as nucleation sites and trigger the rapid formation of Na-based products (N-A-S-H gels) [64]. Besides, since Si ions existing around the fly ash particle would preferentially react with Ca ions to form (C, N)-A-S-H gels, the dissolution rate of fly ash is accelerated to maintain the concentration of Si ions [16]. The formation of (C, N)-A-S-H gels would also consume water, and thus increase the alkalinity of solution around fly ash particle and further encourage its dissolution [16]. Nevertheless, the presence of fly ash has no obvious effect on the microstructure evolution of slag even at later curing ages (7 – 28 d), where the microstructure of slag close to the fly ash particle in AAFS changes steadily, in consistence with the microstructure evolution of isolated slag.

5. Conclusions

In this study, the microstructure evolution of fly ash and slag particles in AAFS paste cured at ambient temperature with curing age is investigated using in-situ X-ray microcomputed tomography (XCT) along with backscattered electron (BSE) and energy dispersive X-ray spectrometer (EDS). Based on the experimental results, the main conclusions can be drawn as follows:

- The dissolution of fly ash and slag particles presents some homogeneity at early ages but tends to be non-uniform at later curing ages due to their inherently heterogeneous characteristics. The non-uniform dissolution of fly ash particle can be mainly attributed to the heterogeneous chemical composition, while the preferential dissolution of slag can be associated with the initial defects induced during the preparation of AAFS sample.
- The formation of reaction products mostly accumulates within the boundary of the original fly ash and slag particles, i.e., the formation of inner products, as a result of the rapid dissolution of etch pits on the particle surface, which would increase the ionic concentration inside the pits and promote the formation of inner products. The inner reaction products would naturally build a physical barrier between the unreacted particles and the outside solution, which would inhibit the further reactions of fly ash and slag particles in AAFS.
- The microstructure evolution of fly ash and slag particles is significantly affected by their structure and size. The dissolution of hollow fly ash particle is faster than that of solid fly ash particle, due to the simultaneous reactions from the outside in and from the inside out. The fly ash and slag particles with a smaller size exhibit a faster dissolution compared to the larger particles because of the relatively high specific area. The dissolution of particles with a relatively large size is easier to become asymmetrical than that of the particles with a smaller

size.

- The interactions between fly ash and slag particles exist in AAFS during chemical reactions with the increase of curing age. The presence of slag would strongly accelerate the microstructure evolution of fly ash at later curing ages (7 – 28 d), which can be ascribed to the diffusion of Ca ions from the dissolved slag to the unreacted fly ash, promoting the reaction rate and the extent of fly ash.

Acknowledgements

The authors gratefully acknowledge the financial support from the Engineering and Physical Sciences Research Council (EPSRC), UK under Grant No. EP/R041504/1 and the Royal Society, UK under Award No. IEC\NSFC\191417 as well as the Visiting Researcher Fund Program of State Key Laboratory of Water Resources and Hydropower Engineering Science, China under Award No. 2019SGG01. The financial support provided by University College London (UCL) and China Scholarship Council (CSC) to the first author is also gratefully acknowledged.

References

[1] Provis JL, van Deventer JSJ. Alkali activated materials: State-of-the-art report, RILEM TC 224-AAM. Netherlands: Springe; 2014.

[2] Fang G, Ho W, Tu W, Zhang M. Workability and mechanical properties of alkali-activated fly ash-slag concrete cured at ambient temperature. Construction and Building Materials. 2018;172:476-87.

[3] Li N, Shi C, Zhang Z, Wang H, Liu Y. A review on mixture design methods for geopolymer concrete. Composites Part B: Engineering. 2019;178:107490.

[4] Fan X, Zhang M. Behaviour of inorganic polymer concrete columns reinforced with basalt FRP bars under eccentric compression: An experimental study. Composites Part B: Engineering. 2016;104:44-56.

[5] Ismail I, Bernal SA, Provis JL, San Nicolas R, Hamdan S, van Deventer JSJ. Modification of phase evolution in alkali-activated blast furnace slag by the incorporation of fly ash. Cement and Concrete Composites. 2014;45:125-35.

[6] Marjanović N, Komljenović M, Baščarević Z, Nikolić V, Petrović R. Physical–mechanical and microstructural properties of alkali-activated fly ash–blast furnace slag blends. Ceramics International. 2015;41(1, Part B):1421-35.

[7] Lee NK, Lee HK. Reactivity and reaction products of alkali-activated, fly ash/slag paste. Construction and Building Materials. 2015;81:303-12.

[8] Ma Y, Yang X, Hu J, Zhang Z, Wang H. Accurate determination of the “time-zero” of autogenous shrinkage in alkali-activated fly ash/slag system. Composites Part B: Engineering. 2019;177:107367.

[9] Puertas F, Martínez-Ramírez S, Alonso S, Vázquez T. Alkali-activated fly ash/slag cements: Strength behaviour and hydration products. Cement Concrete Res. 2000;30(10):1625-32.
[10] Ke X, Duan Y. Coupling machine learning with thermodynamic modelling to develop a composition-property model for alkali-activated materials. Composites Part B: Engineering. 2021;216:108801.
[11] Antonić T, Čižmek A, Kosanović C, Subotić B. Dissolution of amorphous aluminosilicate zeolite precursors in alkaline solutions. Part 1. - Kinetics of the dissolution. Journal of the Chemical Society, Faraday Transactions. 1993;89(11):1817-22.
[12] Hajimohammadi A, van Deventer JSJ. Dissolution behaviour of source materials for synthesis of geopolymer binders: A kinetic approach. International Journal of Mineral Processing. 2016;153:80-6.
[13] Hajimohammadi A, Provis JL, van Deventer JSJ. Effect of Alumina Release Rate on the Mechanism of Geopolymer Gel Formation. Chemistry of Materials. 2010;22(18):5199-208.
[14] Brouwers HJH, Van Eijk RJ. Fly ash reactivity: Extension and application of a shrinking core model and thermodynamic approach. Journal of Materials Science. 2002;37(10):2129-41.
[15] Fernández-Jiménez A, Palomo A, Criado M. Microstructure development of alkali-activated fly ash cement: a descriptive model. Cement and Concrete Research. 2005;35(6):1204-9.
[16] Puligilla S, Mondal P. Role of slag in microstructural development and hardening of fly ash-slag geopolymer. Cement and Concrete Research. 2013;43:70-80.
[17] Pacheco-Torgal F, Labrincha JA, Leonelli C, Palomo A, Chindaprasirt P. Handbook of alkali-activated cements, mortars and concretes: Woodhead Publishing; 2014.
[18] Ye H, Radlińska A. Fly ash-slag interaction during alkaline activation: Influence of activators on phase assemblage and microstructure formation. Construction and Building Materials. 2016;122:594-606.
[19] Durdziński PT, Dunant CF, Haha MB, Scrivener KL. A new quantification method based on SEM-EDS to assess fly ash composition and study the reaction of its individual components in hydrating cement paste. Cement and Concrete Research. 2015;73:111-22.
[20] Gebregziabiher BS, Thomas R, Peethamparan S. Very early-age reaction kinetics and microstructural development in alkali-activated slag. Cement and Concrete Composites. 2015;55:91-102.
[21] Brisard S, Serdar M, Monteiro PJM. Multiscale X-ray tomography of cementitious materials: A review. Cement and Concrete Research. 2020;128:105824.
[22] Landis EN, Keane DT. X-ray microtomography. Materials Characterization. 2010;61(12):1305-16.
[23] Xue G, Yilmaz E, Song W, Cao S. Analysis of internal structure behavior of fiber reinforced

cement-tailings matrix composites through X-ray computed tomography. Composites Part B: Engineering. 2019;175:107091.
[24] Hu Q, Aboustait M, Kim T, Ley MT, Bullard JW, Scherer G, et al. Direct measurements of 3d structure, chemistry and mass density during the induction period of C3s hydration. Cement and Concrete Research. 2016;89:14-26.
[25] Gastaldi D, Canonico F, Capelli L, Boccaleri E, Milanesio M, Palin L, et al. In situ tomographic investigation on the early hydration behaviors of cementing systems. Construction and Building Materials. 2012;29:284-90.
[26] Adrien J, Meille S, Tadier S, Maire E, Sasaki L. In-situ X-ray tomographic monitoring of gypsum plaster setting. Cement and Concrete Research. 2016;82:107-16.
[27] Gallucci E, Scrivener K, Groso A, Stampanoni M, Margaritondo G. 3D experimental investigation of the microstructure of cement pastes using synchrotron X-ray microtomography (μCT). Cement and Concrete Research. 2007;37(3):360-8.
[28] Zhang M, He Y, Ye G, Lange DA, Breugel Kv. Computational investigation on mass diffusivity in Portland cement paste based on X-ray computed microtomography (μCT) image. Construction and Building Materials. 2012;27(1):472-81.
[29] Zhang M. Pore-scale modelling of relative permeability of cementitious materials using X-ray computed microtomography images. Cement and Concrete Research. 2017;95:18-29.
[30] Bossa N, Chaurand P, Vicente J, Borschneck D, Levard C, Aguerre-Chariol O, et al. Micro- and nano-X-ray computed-tomography: A step forward in the characterization of the pore network of a leached cement paste. Cement and Concrete Research. 2015;67:138-47.
[31] Wang L, Yang B, Abraham A, Qi L, Zhao X, Chen Z. Construction of dynamic three-dimensional microstructure for the hydration of cement using 3D image registration. Pattern Analysis and Applications. 2014;17(3):655-65.
[32] Provis JL, Myers RJ, White CE, Rose V, van Deventer JSJ. X-ray microtomography shows pore structure and tortuosity in alkali-activated binders. Cement and Concrete Research. 2012;42(6):855-64.
[33] Rivera OG, Long WR, Weiss Jr CA, Moser RD, Williams BA, Torres-Cancel K, et al. Effect of elevated temperature on alkali-activated geopolymeric binders compared to portland cement-based binders. Cement and Concrete Research. 2016;90:43-51.
[34] Borges PHR, Banthia N, Alcamand HA, Vasconcelos WL, Nunes EHM. Performance of blended metakaolin/blastfurnace slag alkali-activated mortars. Cement and Concrete Composites. 2016;71:42-52.
[35] Zhu X, Zhang Z, Yang K, Magee B, Wang Y, Yu L, et al. Characterisation of pore structure development of alkali-activated slag cement during early hydration using electrical responses.

Cement and Concrete Composites. 2018;89:139-49.
[36] Provis JL, Rose V, Winarski RP, van Deventer JSJ. Hard X-ray nanotomography of amorphous aluminosilicate cements. Scripta Materialia. 2011;65(4):316-9.
[37] Fang G, Ho WK, Tu W, Zhang M. Workability and mechanical properties of alkali-activated fly ash-slag concrete cured at ambient temperature. Construction and Building Materials. 2018;172:476-87.
[38] Nath P, Sarker PK. Effect of GGBFS on setting, workability and early strength properties of fly ash geopolymer concrete cured in ambient condition. Construction and Building Materials. 2014;66:163-71.
[39] Lee NK, Lee HK. Setting and mechanical properties of alkali-activated fly ash/slag concrete manufactured at room temperature. Construction and Building Materials. 2013;47:1201-9.
[40] Jang JG, Lee NK, Lee HK. Fresh and hardened properties of alkali-activated fly ash/slag pastes with superplasticizers. Construction and Building Materials. 2014;50:169-76.
[41] Talha Junaid M, Kayali O, Khennane A, Black J. A mix design procedure for low calcium alkali activated fly ash-based concretes. Construction and Building Materials. 2015;79:301-10.
[42] BS EN 197-1:2011. Cement part 1: Composition, specifications and conformity criteria for common cements, BSI Standards Publication. 2011.
[43] BS EN 206:2013+A1:2016. Concrete — Specification, performance, production and conformity, BSI Standards Publication. 2016.
[44] Fang G, Zhang M. The evolution of interfacial transition zone in alkali-activated fly ash-slag concrete. Cement and Concrete Research. 2020;129:105963.
[45] Gerward L. X-ray attenuation coefficients: Current state of knowledge and availability. Radiation Physics & Chemistry. 1993;41(4-5):783-9.
[46] McCullough EC. Photon attenuation in computed tomography. Medical Physics. 1975;2(6):307-20.
[47] Buades A, Coll B, Morel JM. A Review of Image Denoising Algorithms, with a New One. Multiscale Modeling & Simulation. 2005;4(2):490-530.
[48] Sauvola J, Pietikäinen M. Adaptive document image binarization. Pattern Recognition. 2000;33(2):225-36.
[49] Fang G, Zhang M. Multiscale micromechanical analysis of alkali-activated fly ash-slag paste. Cement and Concrete Research. 2020;135:106141.
[50] Taiwo OO, Finegan DP, Gelb J, Holzner C, Brett DJL, Shearing PR. The use of contrast enhancement techniques in X-ray imaging of lithium–ion battery electrodes. Chemical Engineering Science. 2016;154:27-33.
[51] Wong HS, Head MK, Buenfeld NR. Pore segmentation of cement-based materials from

backscattered electron images. Cement and Concrete Research. 2006;36(6):1083-90.
[52] Ma L, Fauchille AL, Dowey PJ, Pilz FF, Courtois L, Taylor KG, et al. Correlative multi-scale imaging of shales: a review and future perspectives. Geological Society London Special Publications. 2017:SP454.11.
[53] Kastner J, Harrer B, Requena G, Brunke O. A comparative study of high resolution cone beam X-ray tomography and synchrotron tomography applied to Fe- and Al-alloys. NDT & E International. 2010;43(7):599-605.
[54] Zhang P, Lu S, Li J, Zhang P, Xie L, Xue H, et al. Multi-component segmentation of X-ray computed tomography (CT) image using multi-Otsu thresholding algorithm and scanning electron microscopy. Energy Exploration & Exploitation. 2017;35(3):281-94.
[55] Flatabø R, Coste A, Greve MM. A systematic investigation of the charging effect in scanning electron microscopy for metal nanostructures on insulating substrates. Journal of Microscopy. 2017;265(3):287-97.
[56] Songpiriyakij S, Kubprasit T, Jaturapitakkul C, Chindaprasirt P. Compressive strength and degree of reaction of biomass- and fly ash-based geopolymer. Construction and Building Materials. 2010;24(3):236-40.
[57] Bae S, Meral C, Oh J-e, Moon J, Kunz M, Monteiro PJM. Characterization of morphology and hydration products of high-volume fly ash paste by monochromatic scanning x-ray micro-diffraction (μ-SXRD). Cement and Concrete Research. 2014;59:155-64.
[58] Chancey RT, Stutzman P, Juenger MCG, Fowler DW. Comprehensive phase characterization of crystalline and amorphous phases of a Class F fly ash. Cement and Concrete Research. 2010;40(1):146-56.
[59] Duxson P, Provis JL, Lukey GC, Mallicoat SW, Kriven WM, van Deventer JSJ. Understanding the relationship between geopolymer composition, microstructure and mechanical properties. Colloids and Surfaces A: Physicochemical and Engineering Aspects. 2005;269(1):47-58.
[60] Yin B, Kang T, Kang J, Chen Y. Analysis of Active Ion-Leaching Behavior and the Reaction Mechanism During Alkali Activation of Low-Calcium Fly Ash. International Journal of Concrete Structures and Materials. 2018;12(1):50.
[61] Zuo Y, Ye G. Pore Structure Characterization of Sodium Hydroxide Activated Slag Using Mercury Intrusion Porosimetry, Nitrogen Adsorption, and Image Analysis. Materials. 2018;11(6):1035.
[62] Park S, Abate SY, Lee HK, Kim H-K. On the quantification of degrees of reaction and hydration of sodium silicate-activated slag cements. Materials and Structures. 2020;53(3):65.
[63] Puertas F, Palacios M, Manzano H, Dolado JS, Rico A, Rodríguez J. A model for the C-A-S-H gel formed in alkali-activated slag cements. Journal of the European Ceramic Society.

2011;31(12):2043-56.
[64] Yip CK, Lukey GC, Provis JL, van Deventer JSJ. Effect of calcium silicate sources on geopolymerisation. Cement and Concrete Research. 2008;38(4):554-64.

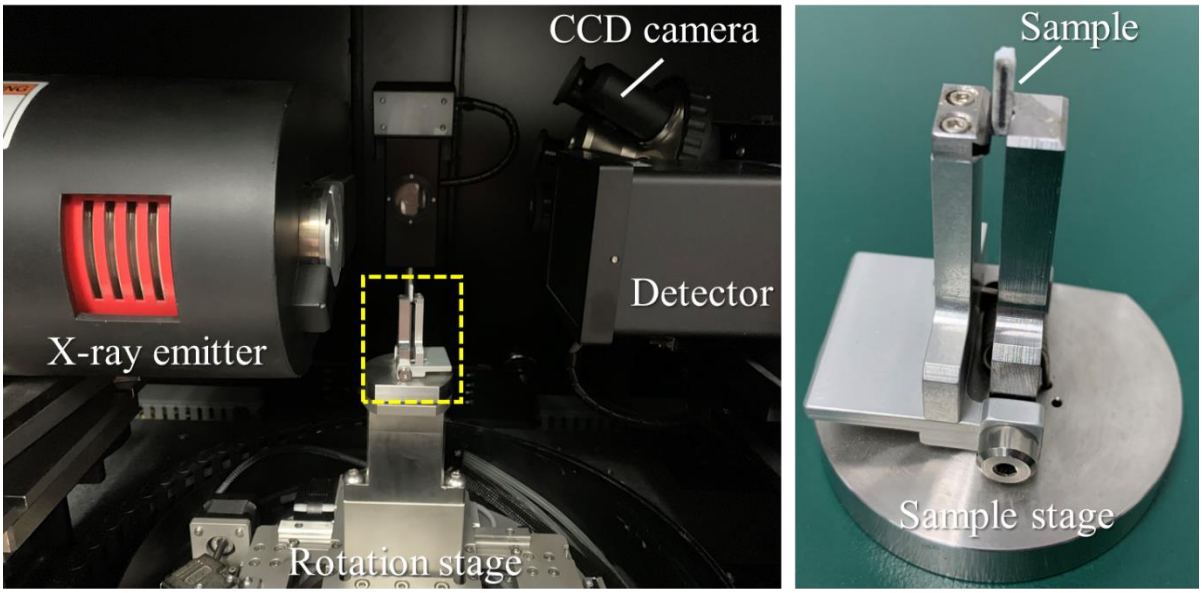

Fig. 1. Experimental setup of X-ray microcomputed tomography (XCT) test

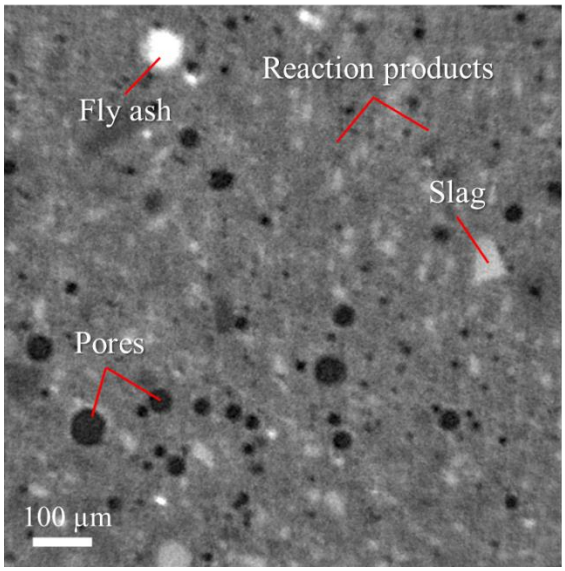

(a) Original image

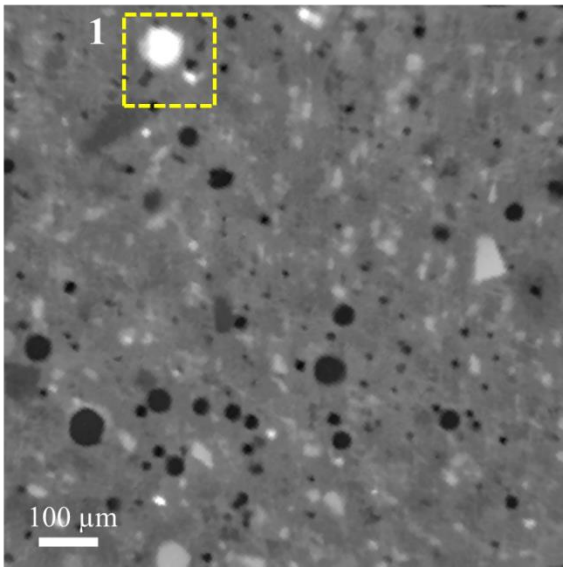

(b) Image after denoising

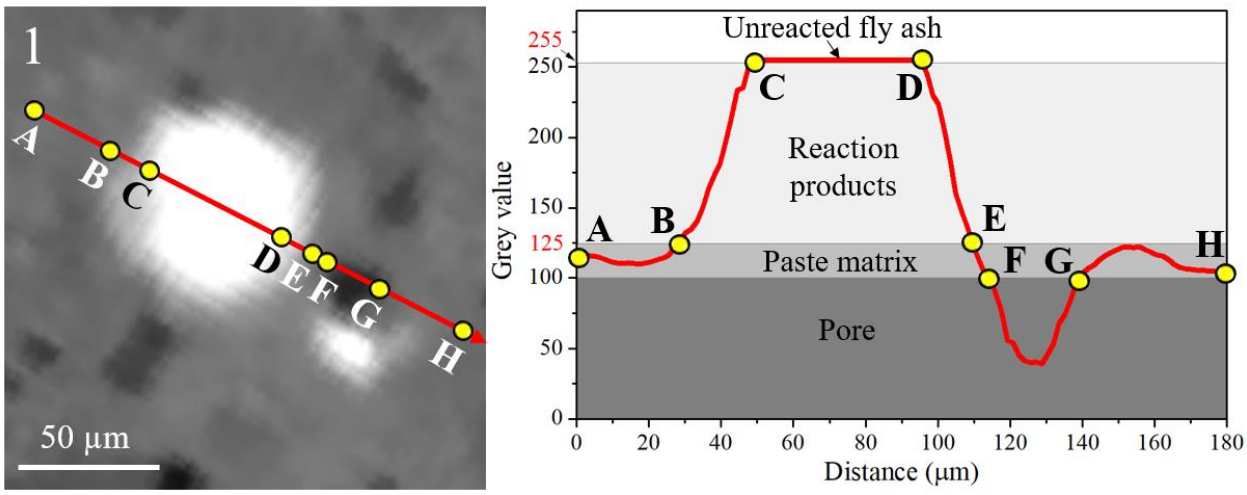

(c) Phases segmentation

Fig. 2. XCT image analysis (t = 1 d)

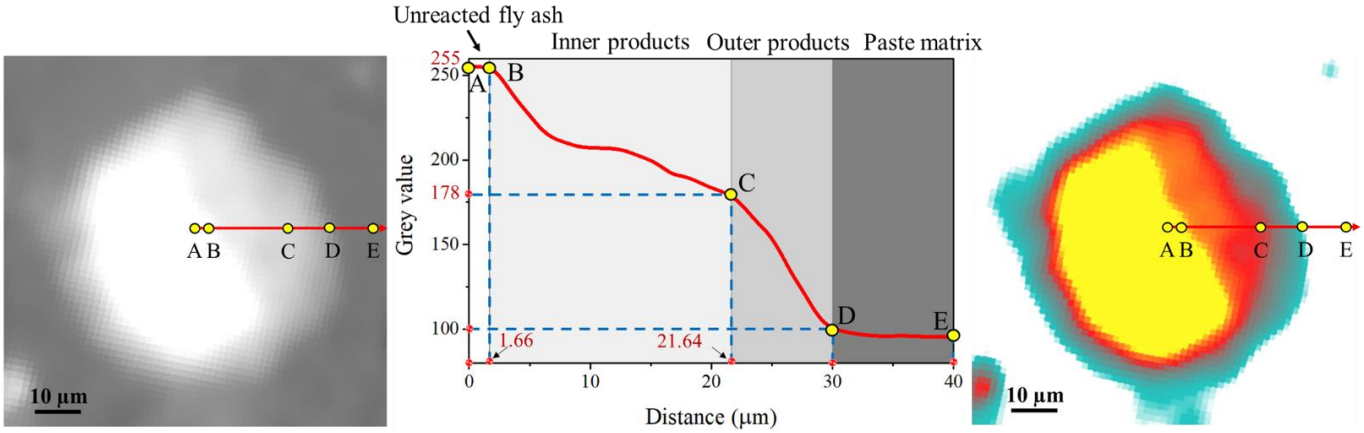

(a) Greyscale image (b) Grey value across fly ash particle (c) Polychromatic image

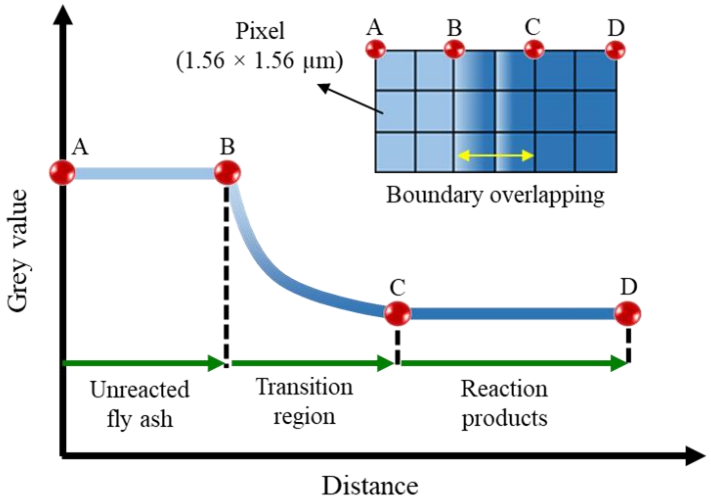

(d) Schematic illustration of the grey value transition region at the boundary between unreacted fly ash and reaction products

Fig. 3. Phase identification of fly ash particle in AAFS mix (t = 28 d)

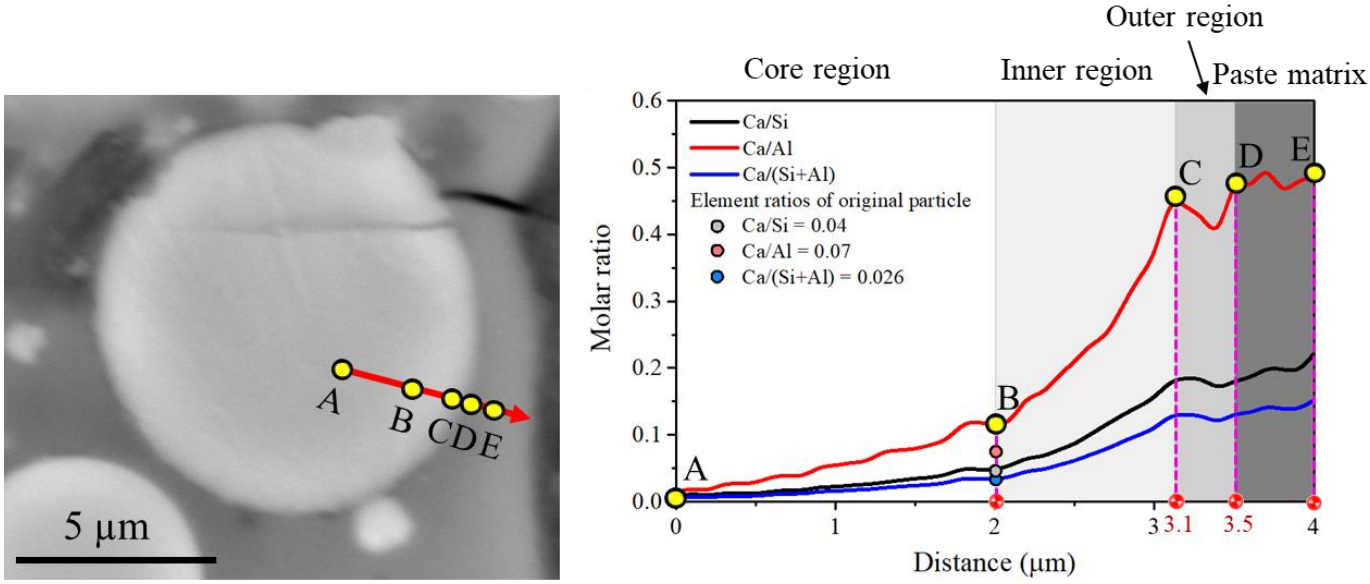

(a) BSEM image (b) Results of EDS line analysis

Fig. 4. Chemical composition of fly ash particle in AAFS mix (t = 28 d)

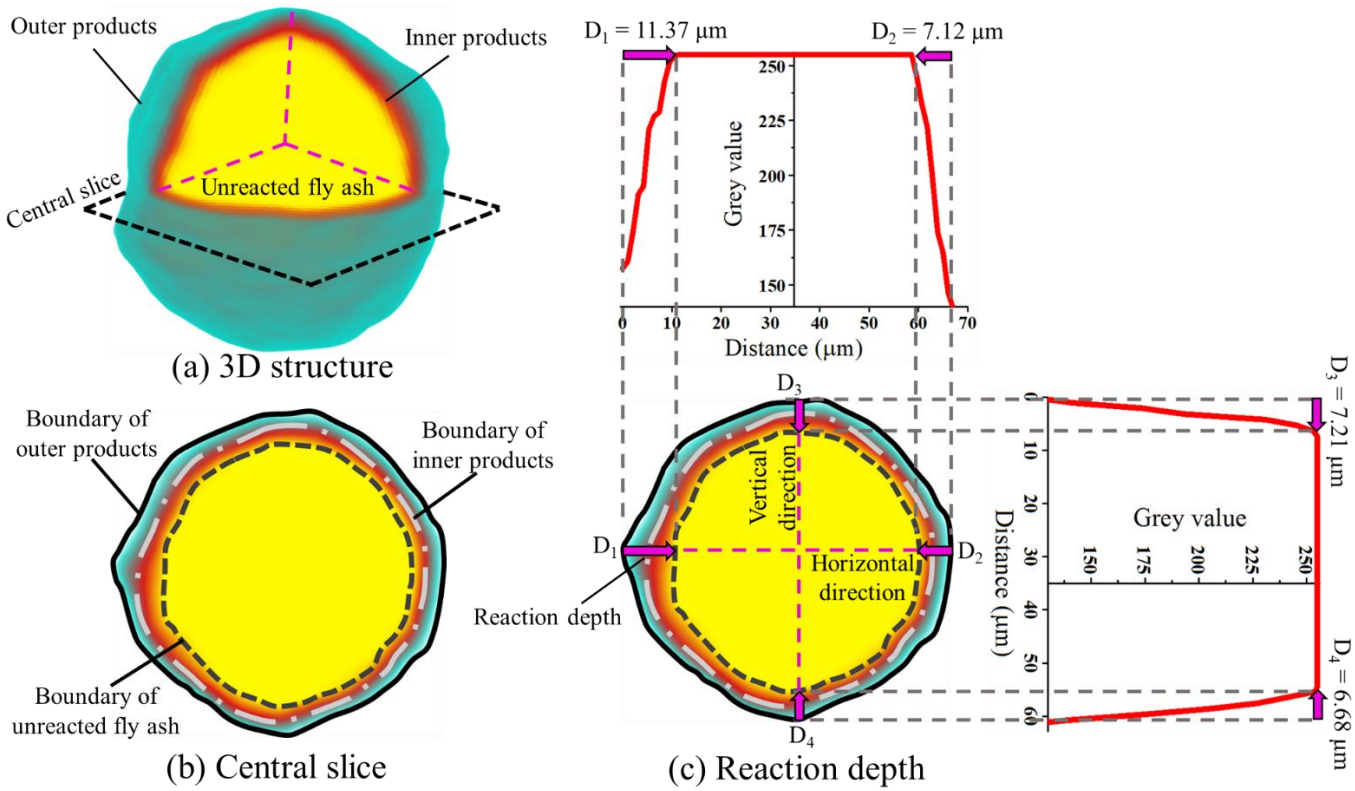

Fig. 5. Feature identification of fly ash particle in AAFS mix (t = 1 d)

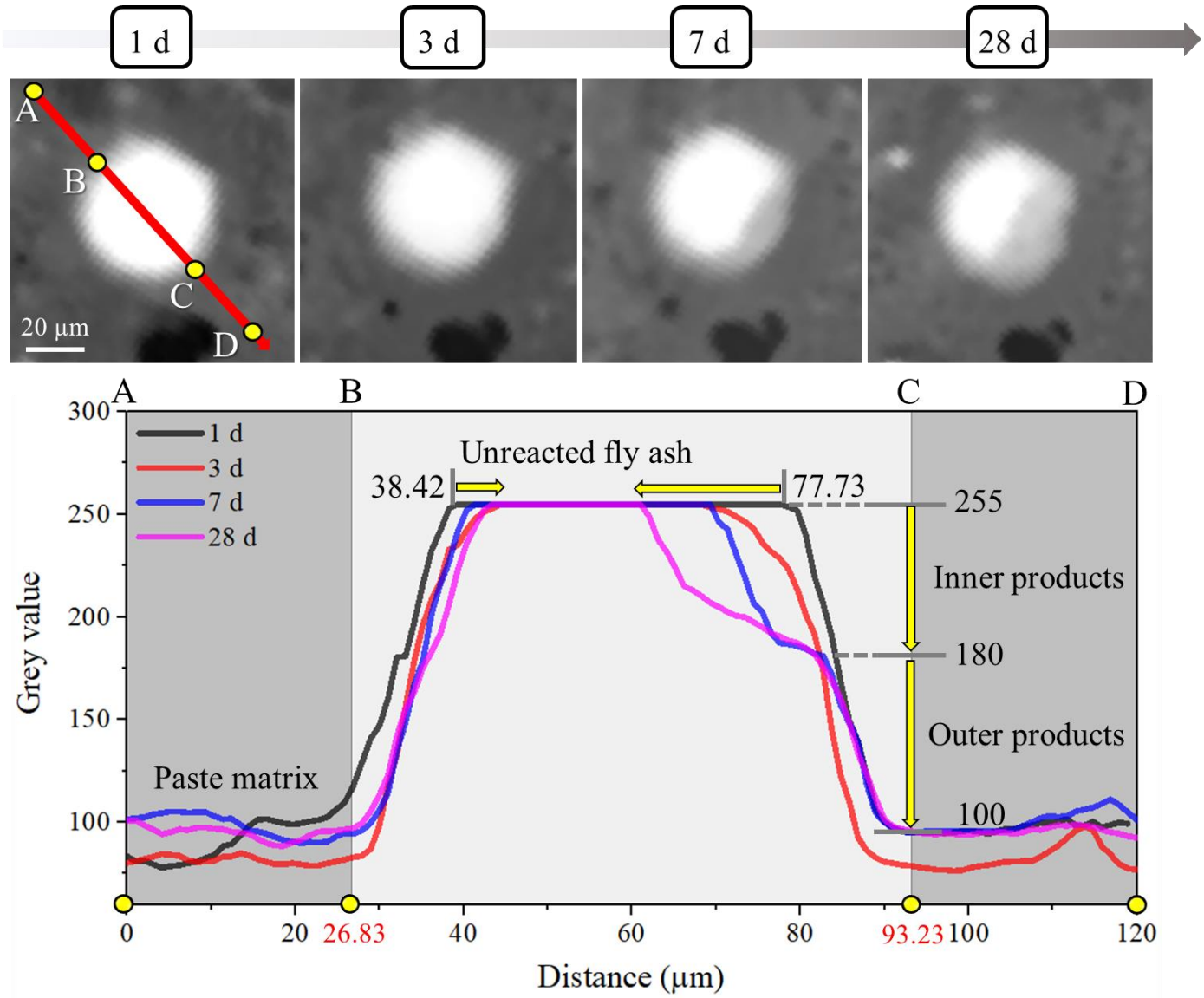

Fig. 6. Grey value across fly ash particle in AAFS mix at different curing ages

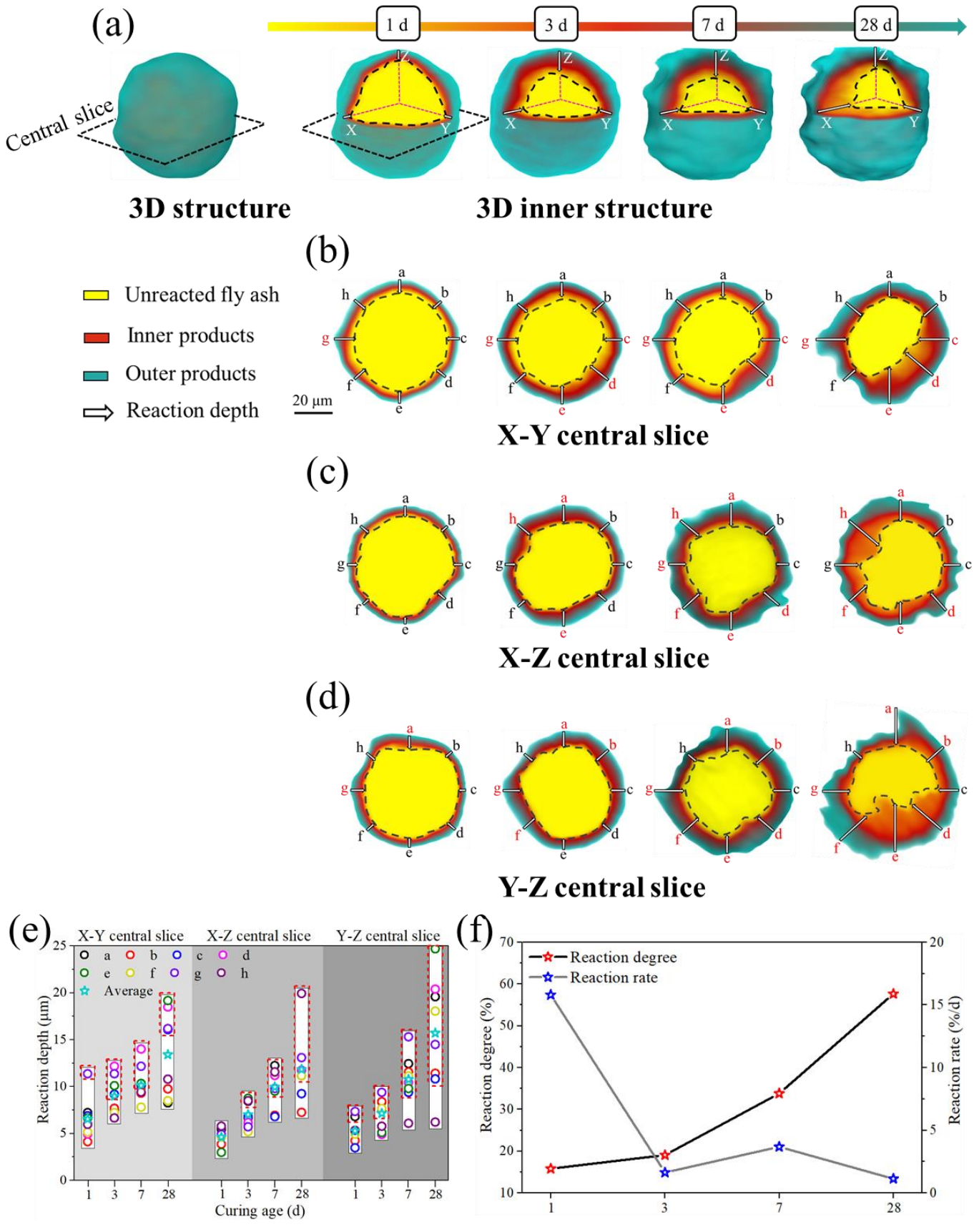

Fig. 7. Reaction depth and reaction degree of fly ash particle in AAFS mix at different curing ages

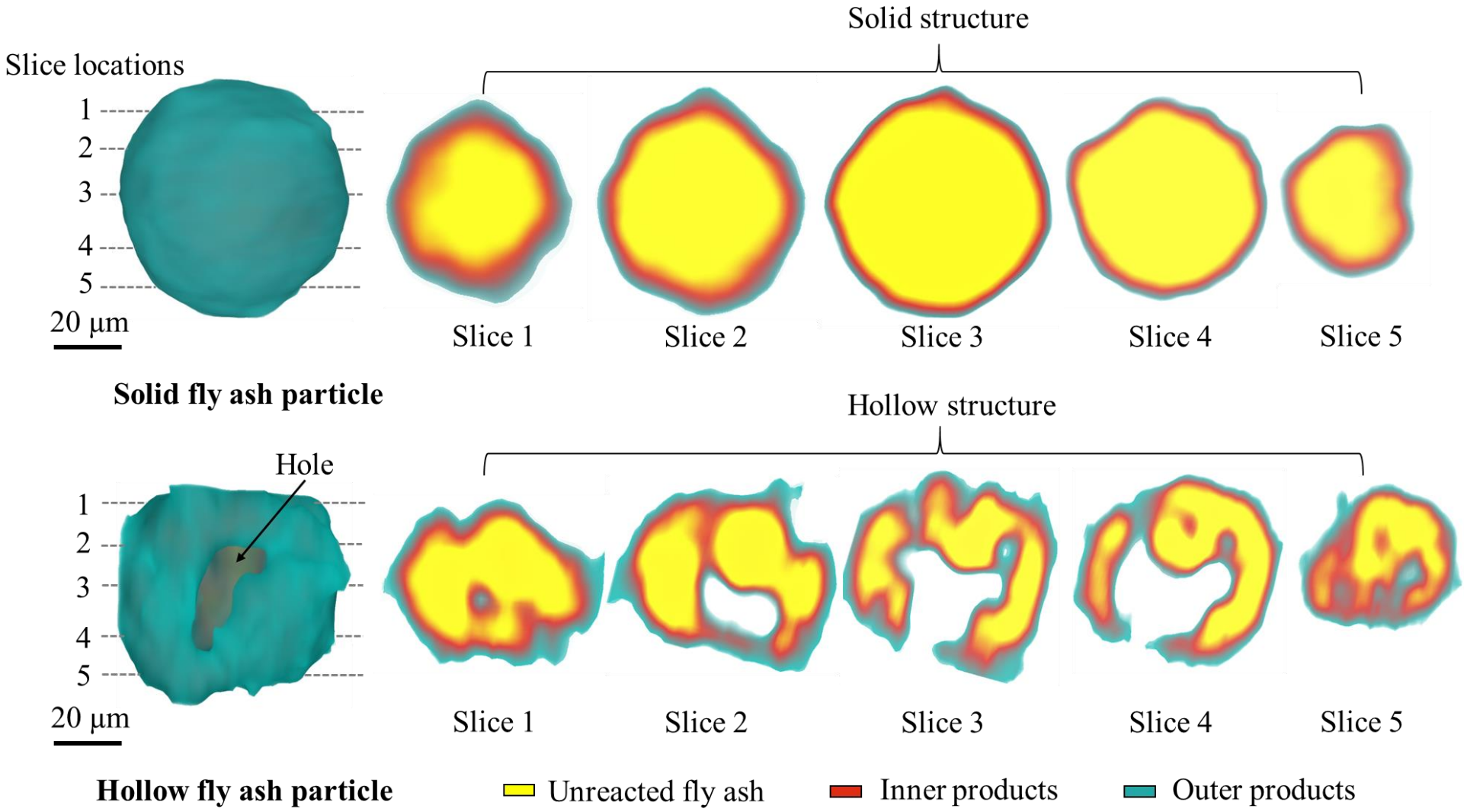

Fig. 8. 2D/3D structure of solid fly ash particle and hollow fly ash particle in AAFS mix (t = 1 d)

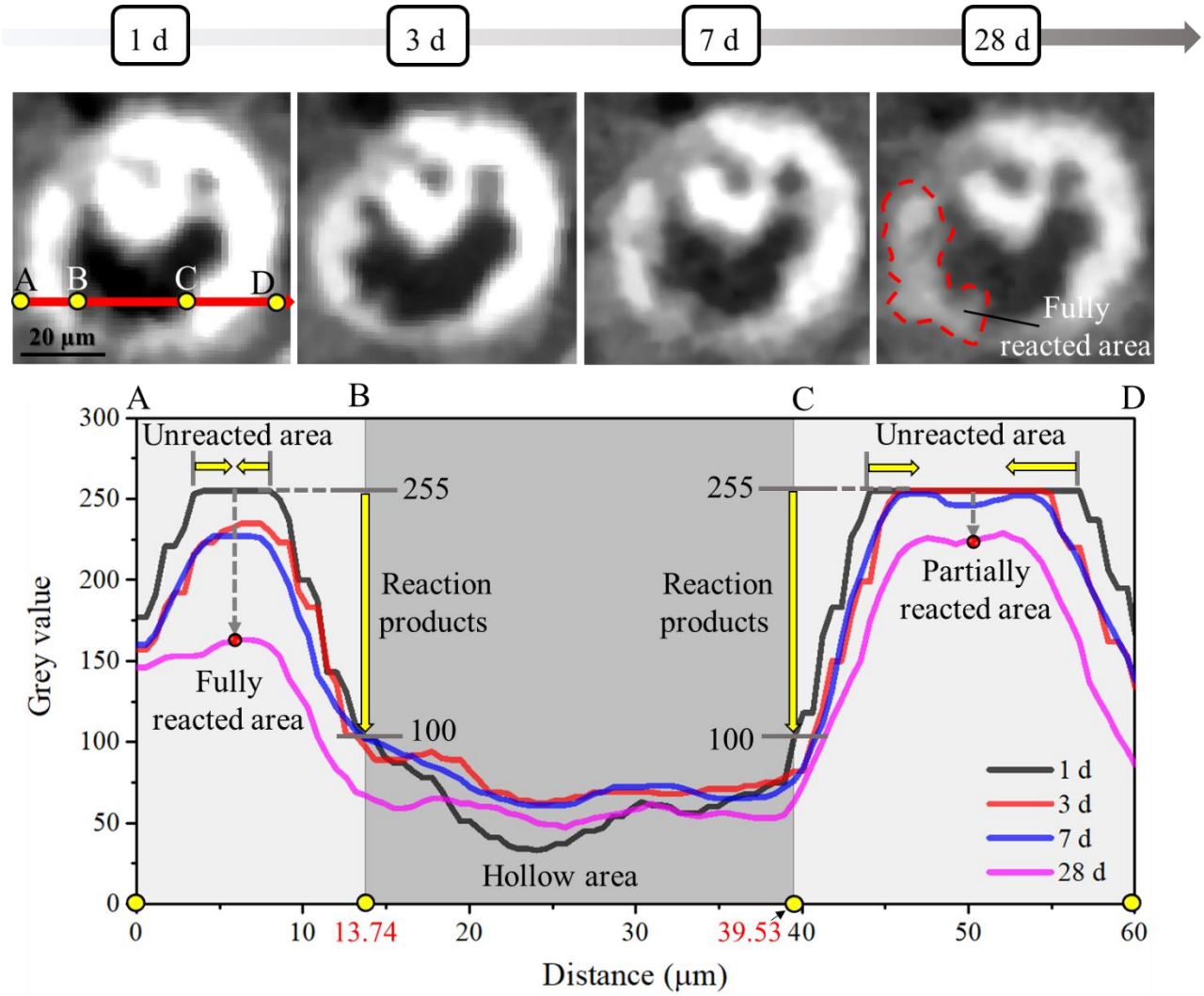

Fig. 9. Grey value across hollow fly ash particle in AAFS mix at different curing ages

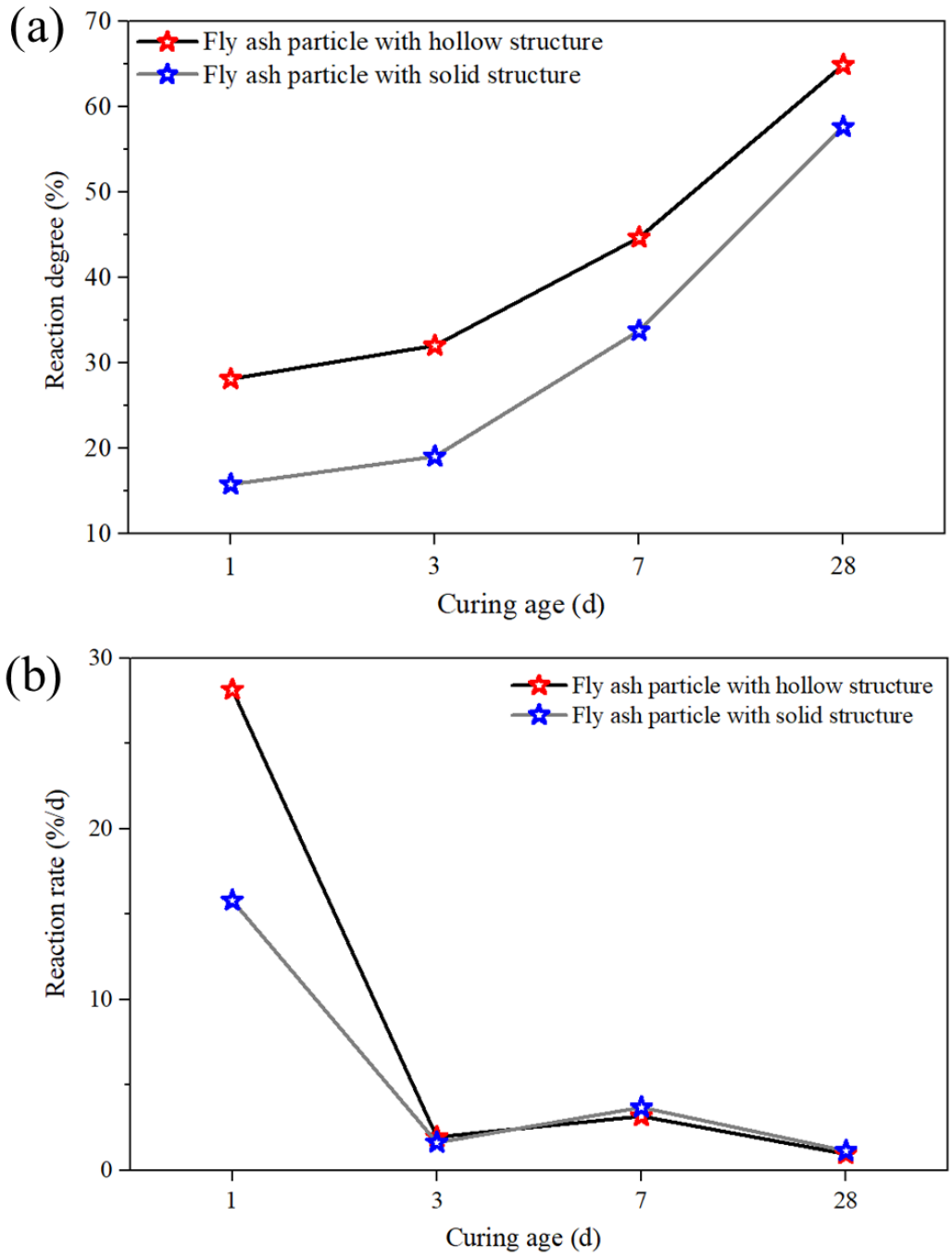

Fig. 10. Reaction degree and reaction rate of solid and hollow fly ash particles in AAFS mix at different curing ages

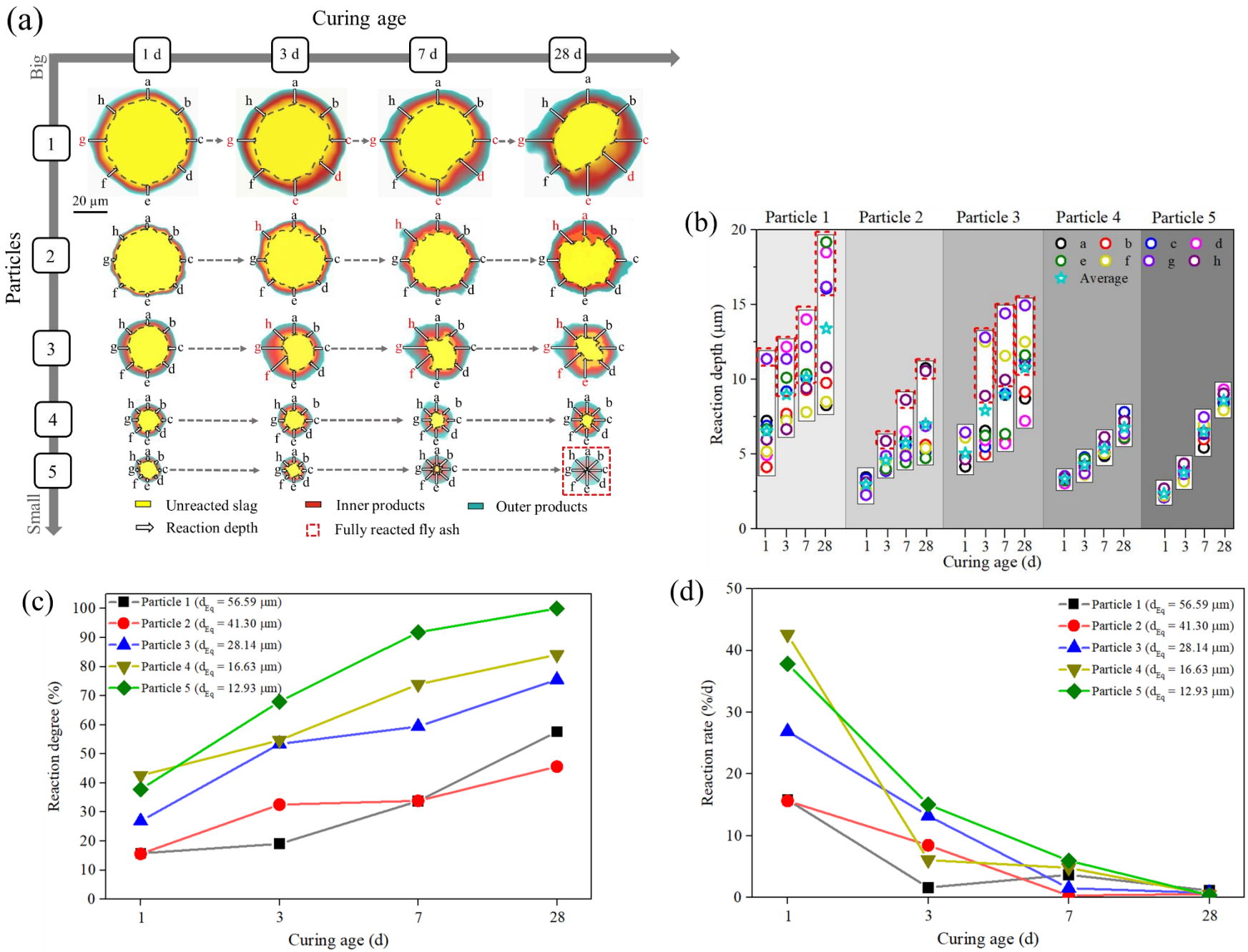

Fig. 11. Reaction depth and reaction degree of fly ash particles with different sizes in AAFS mix at different curing ages

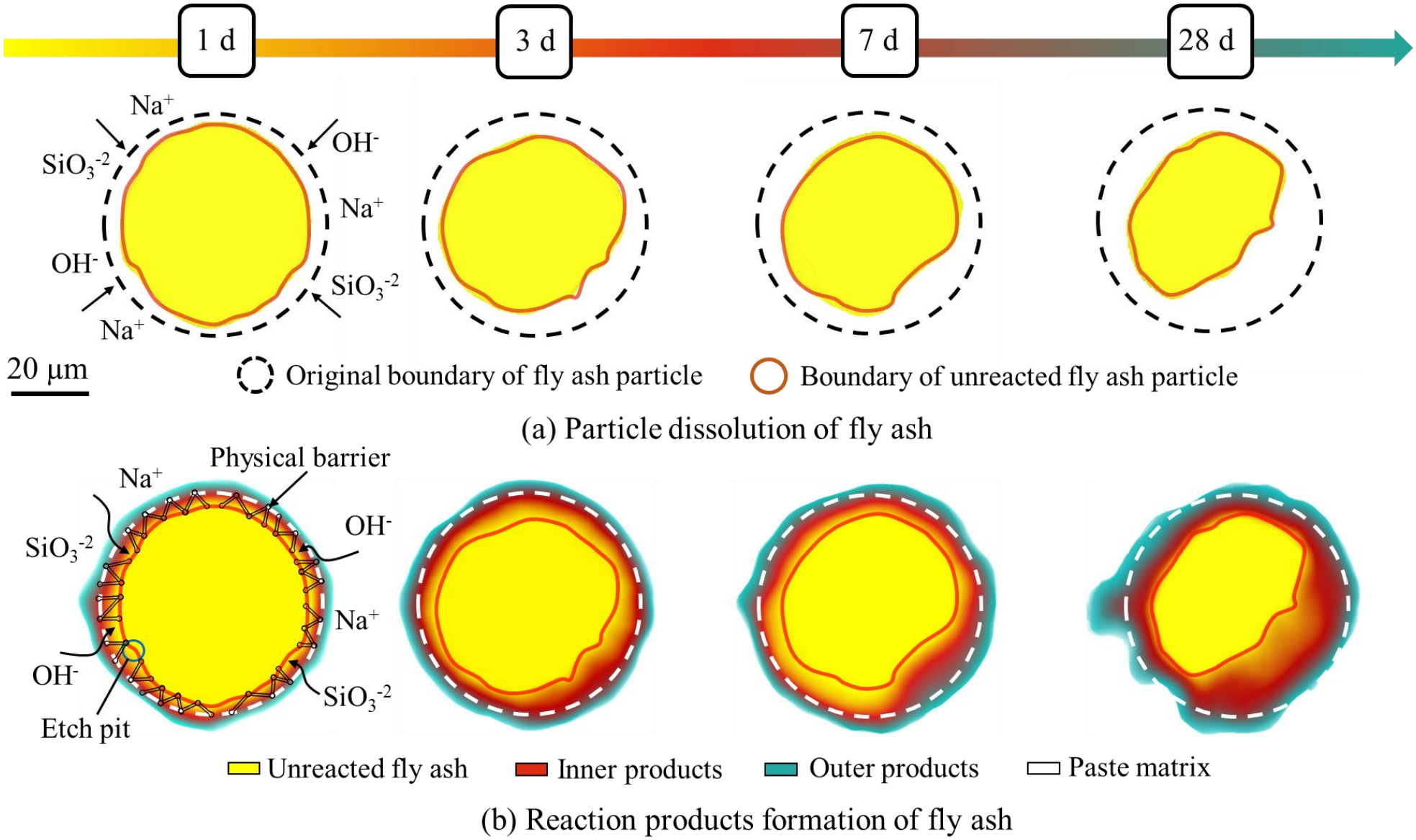

Fig. 12. Microstructure evolution of fly ash particle in AAFS mix

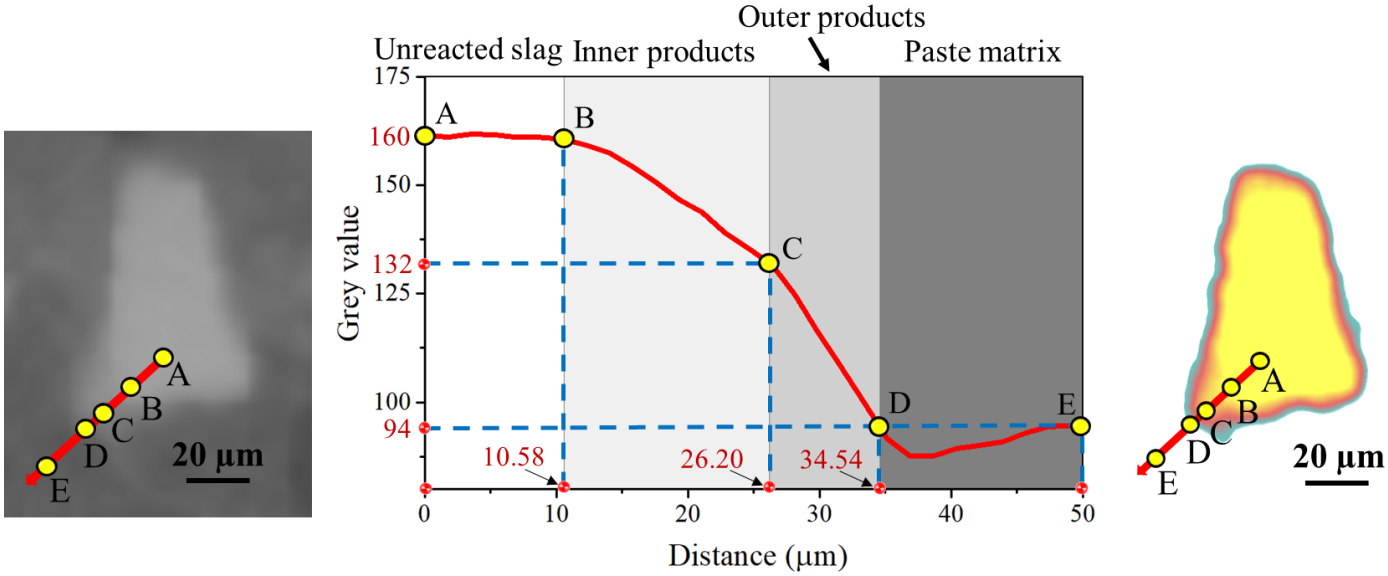

(a) Greyscale image (b) Grey value across slag particle (c) Polychromatic image

Fig. 13. Phase identification of slag particle in AAFS mix (t = 1 d)

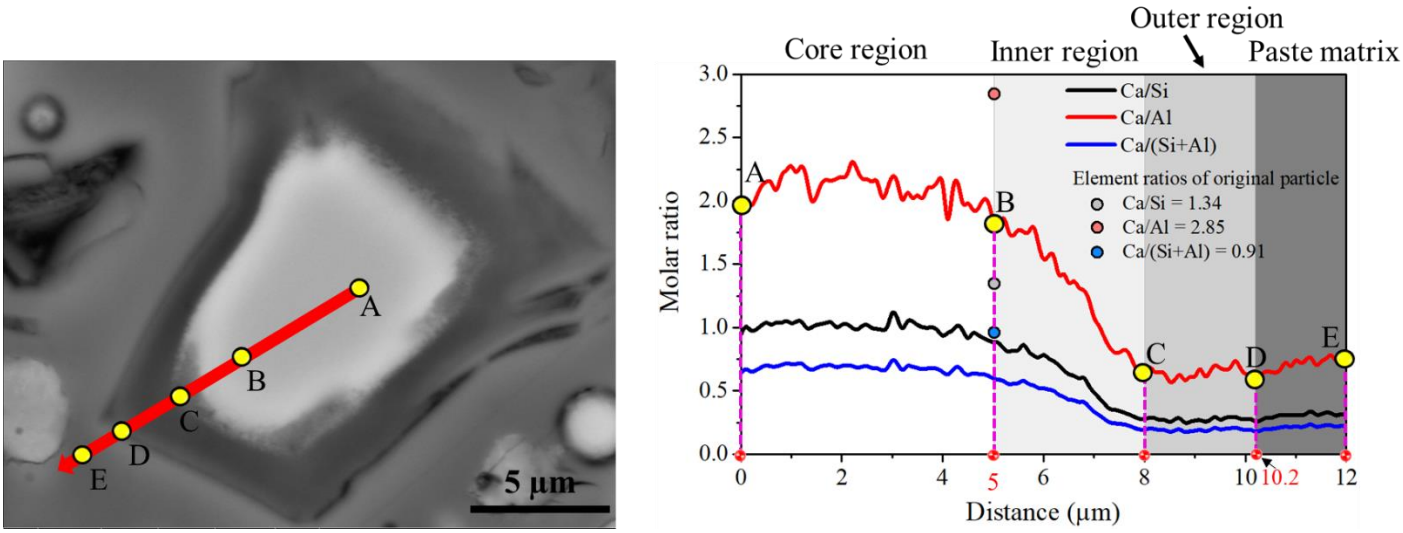

(a) BSEM image (b) Results of EDS line analysis

Fig. 14. Chemical composition of slag particle in AAFS mix (t = 1 d)

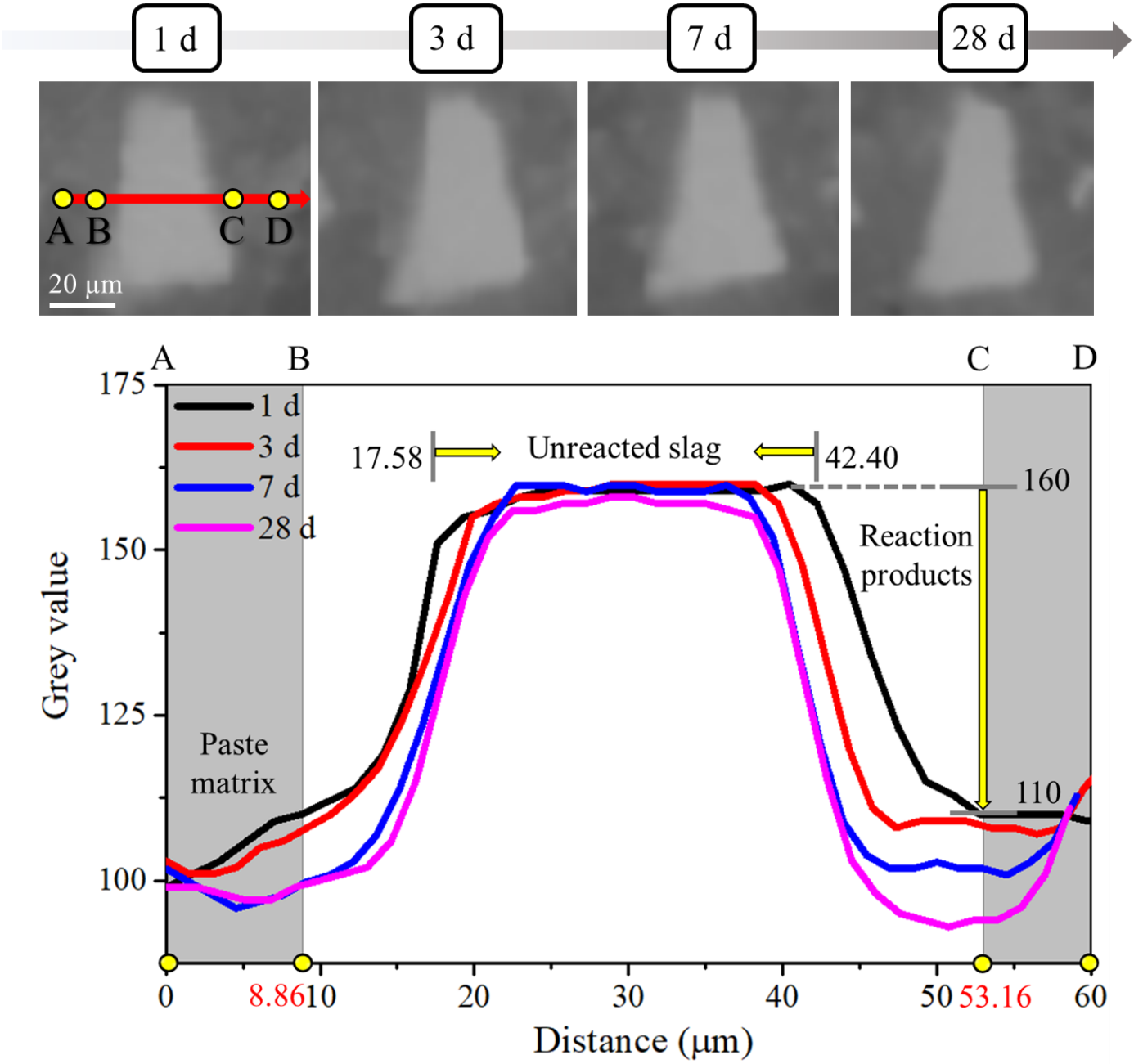

Fig. 15. Grey value across slag particle in AAFS mix at different curing ages

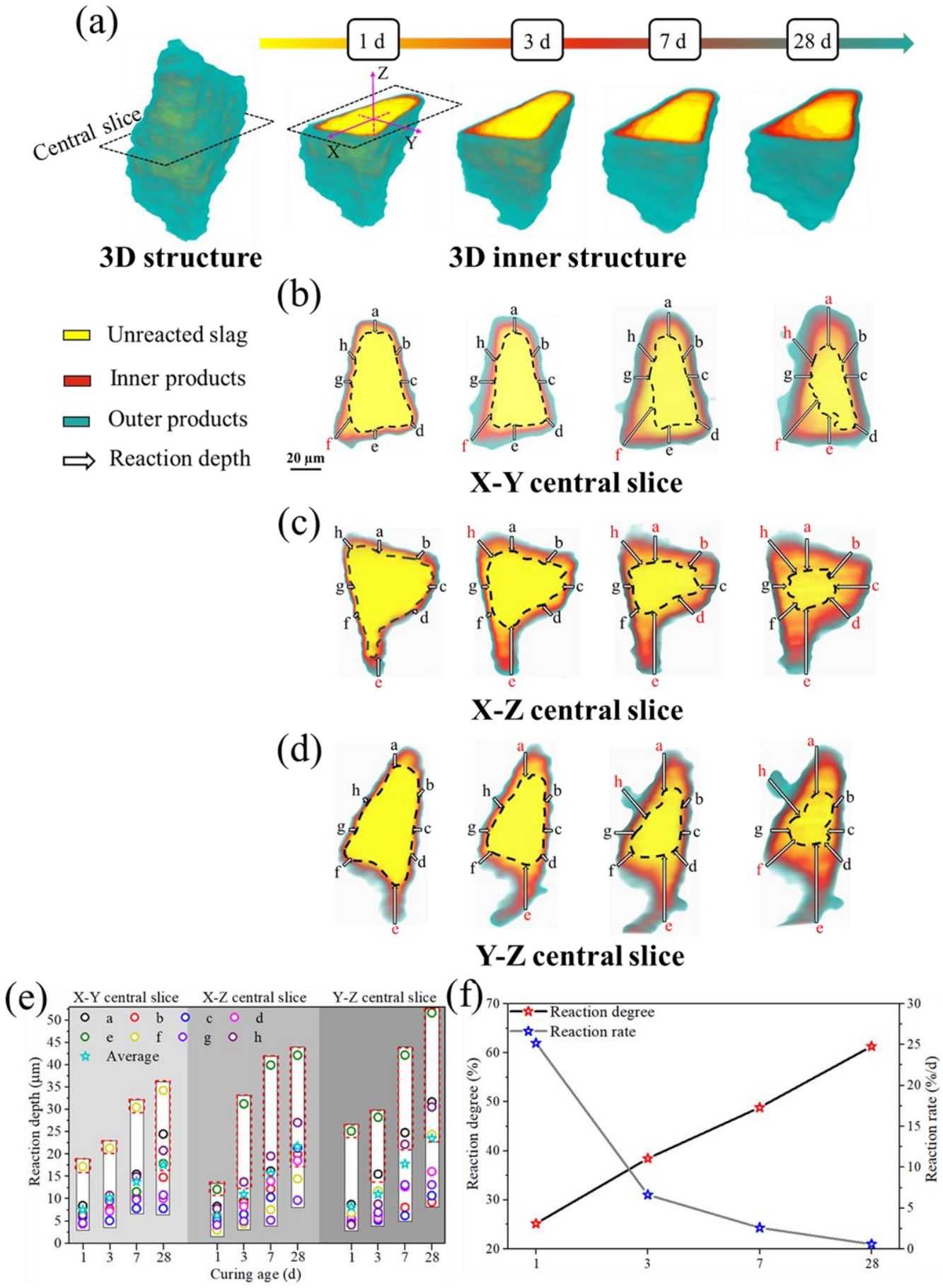

Fig. 16. Reaction depth and reaction degree of slag particle in AAFS mix at different curing ages

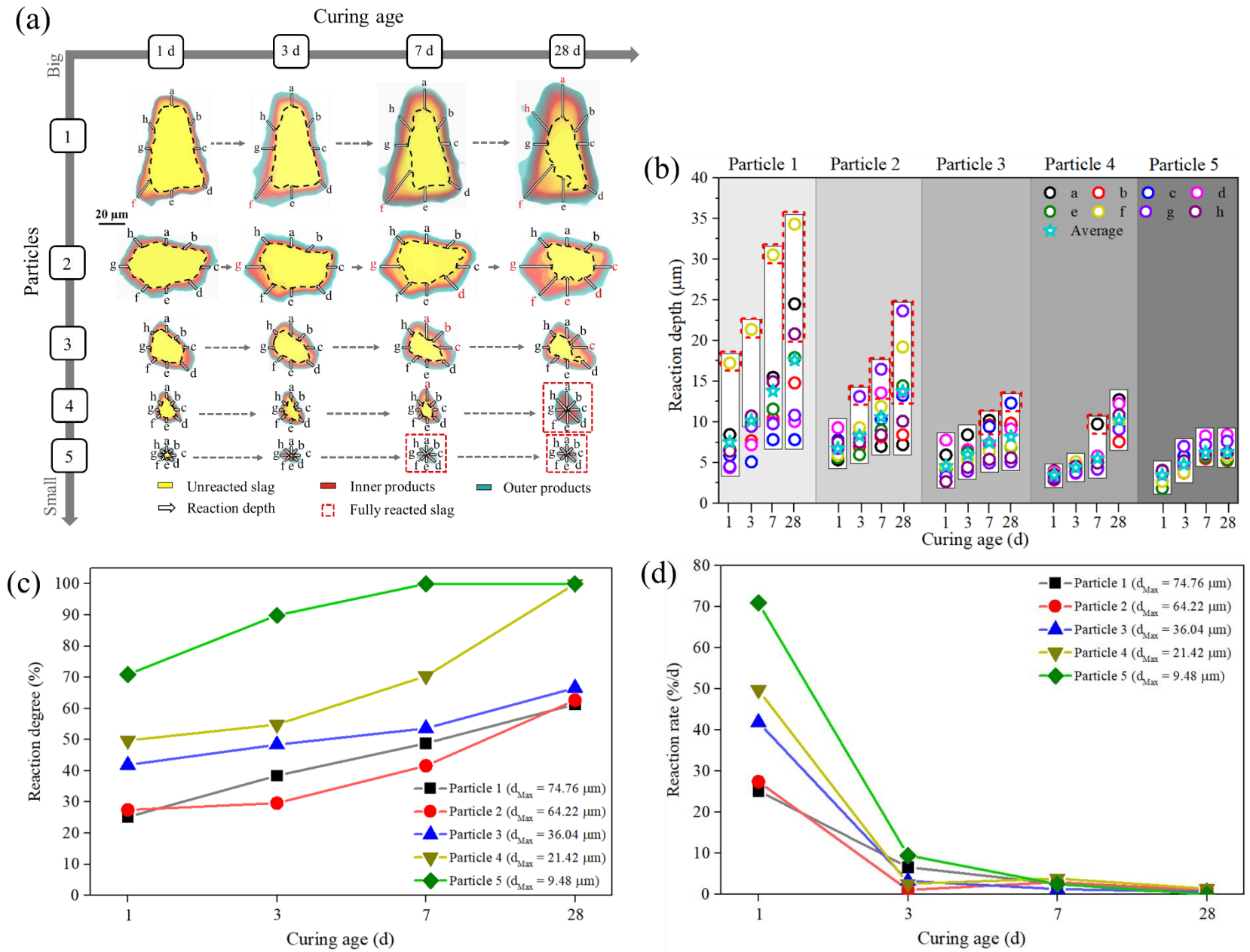

Fig. 17. Reaction depth and reaction degree of slag particles with different sizes in AAFS mix at different curing ages

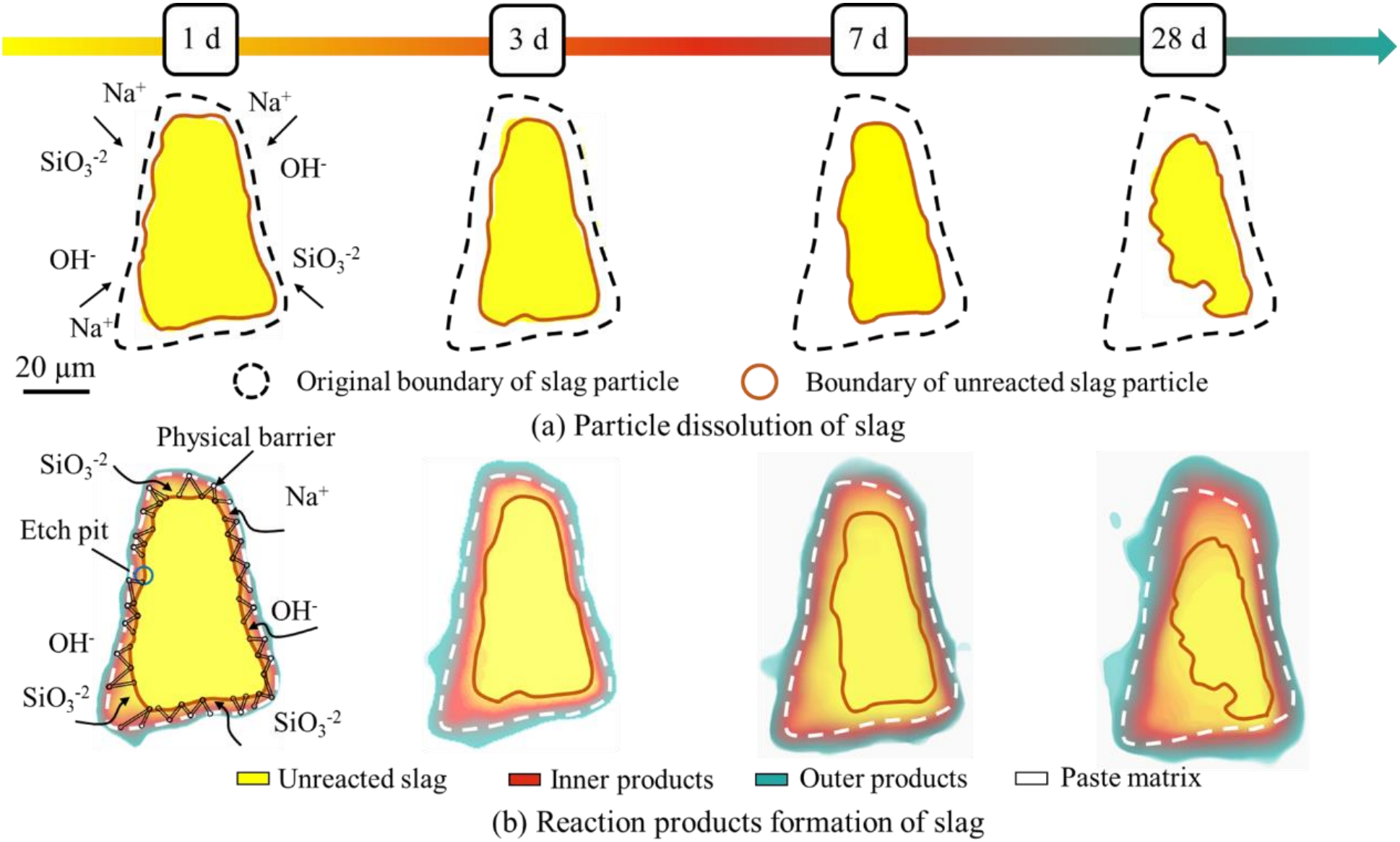

Fig. 18. Microstructure evolution of slag particle in AAFS mix

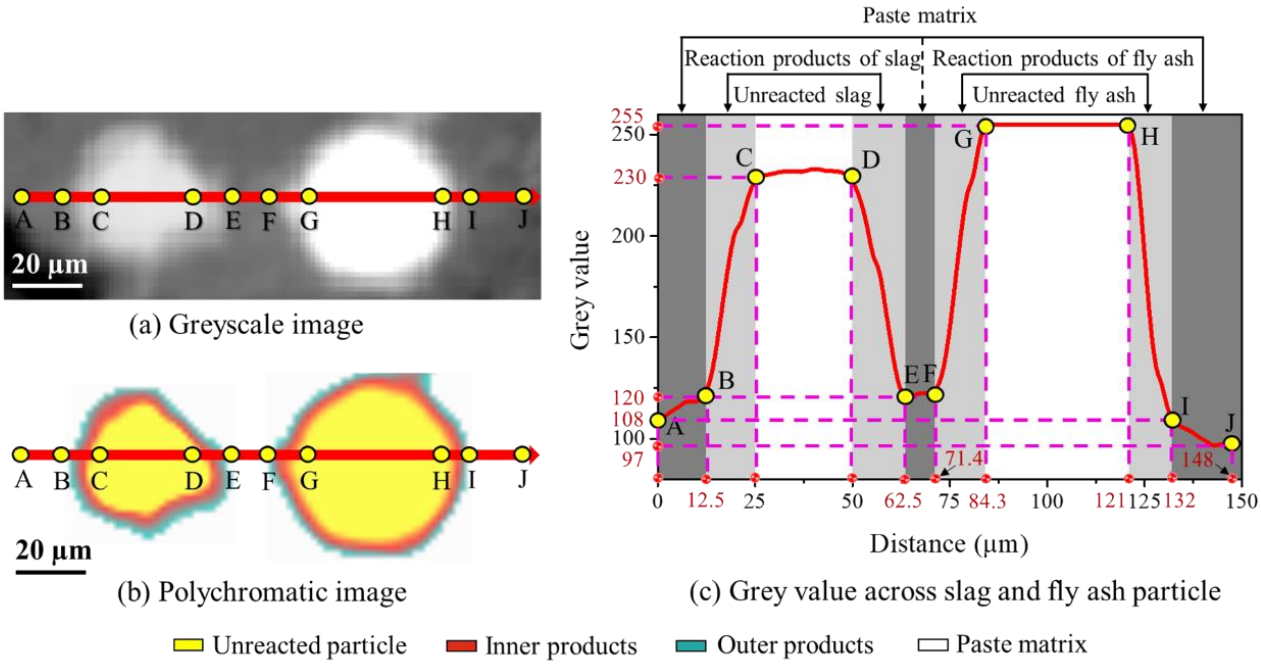

Fig. 19. Phase identification of slag and fly ash particles in AAFS mix (t = 1 d)

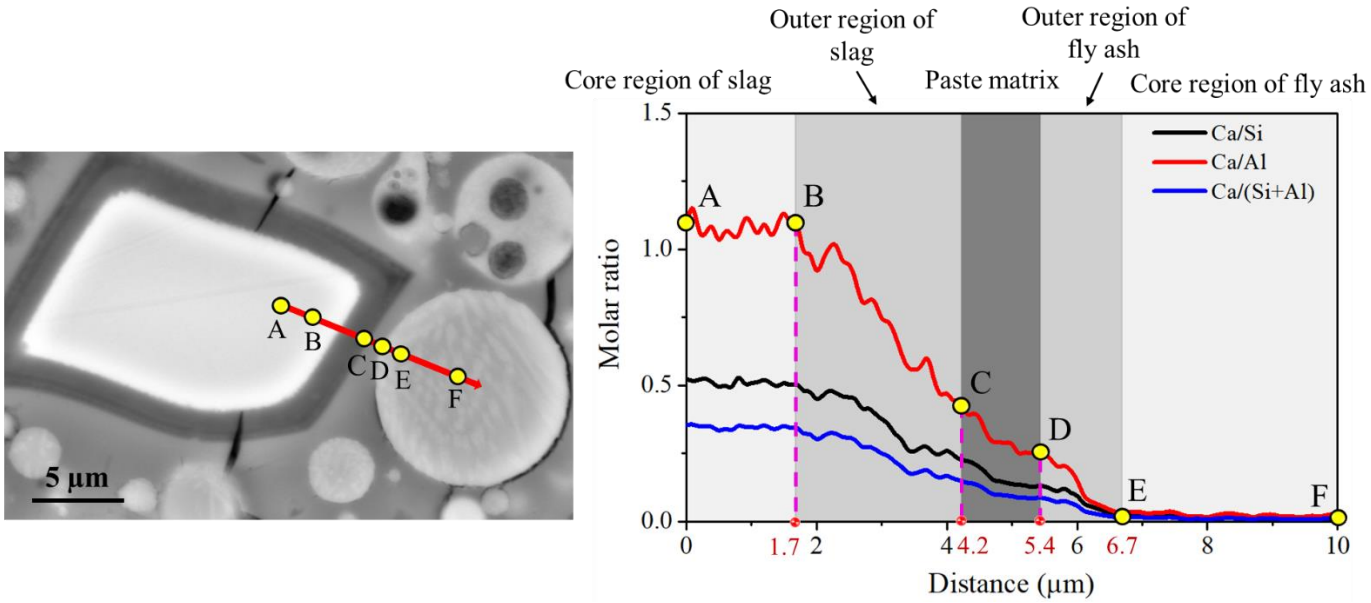

(a) BSEM image (b) Results of EDS line analysis

Fig. 20. Chemical composition across slag and fly ash particle in AAFS mix (t = 28 d)

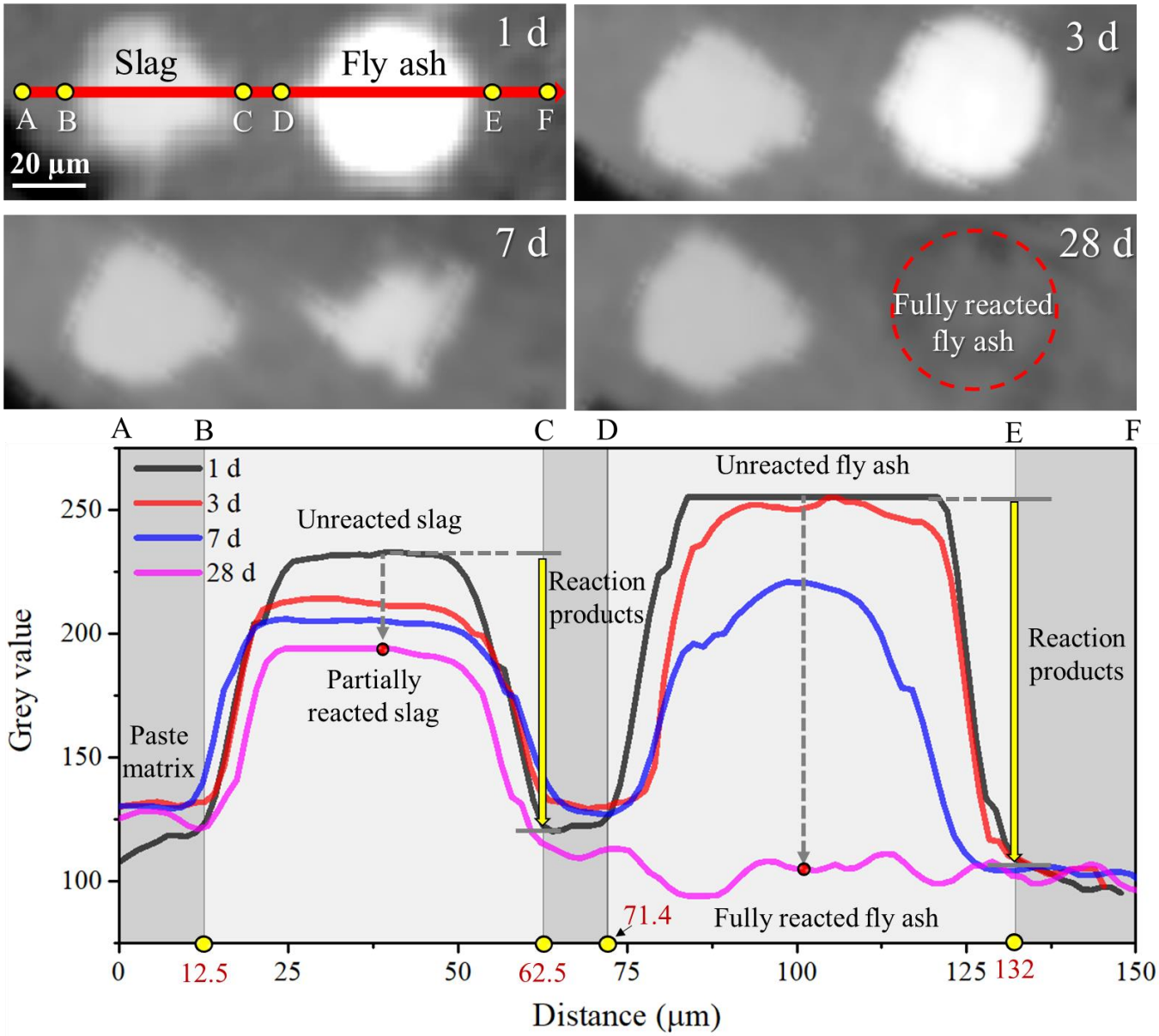

Fig. 21. Grey value across slag and fly ash particles in AAFS mix at different curing ages

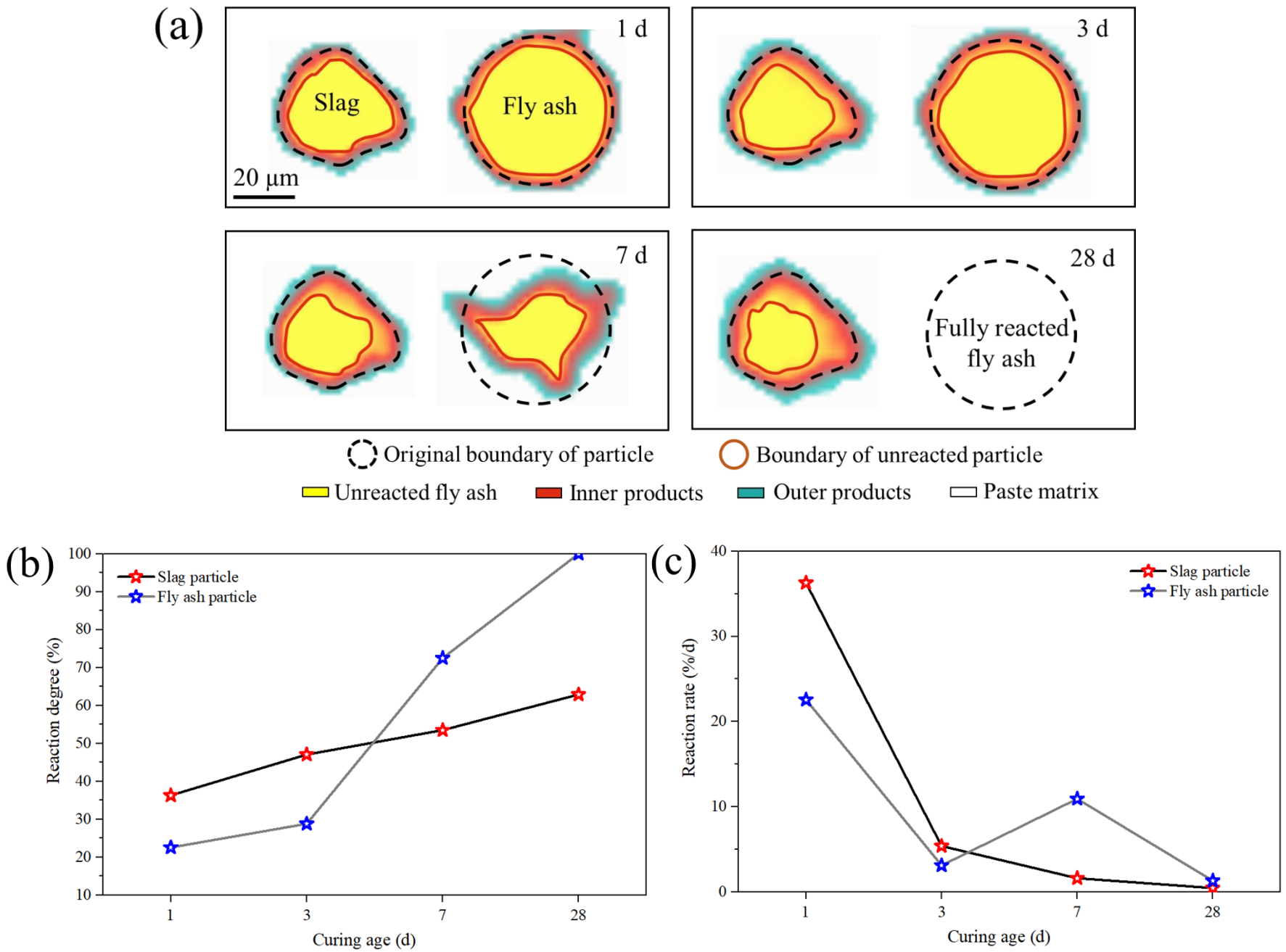

Fig. 22. Reaction degree and reaction rate of slag and fly ash particles in AAFS mix at different curing ages

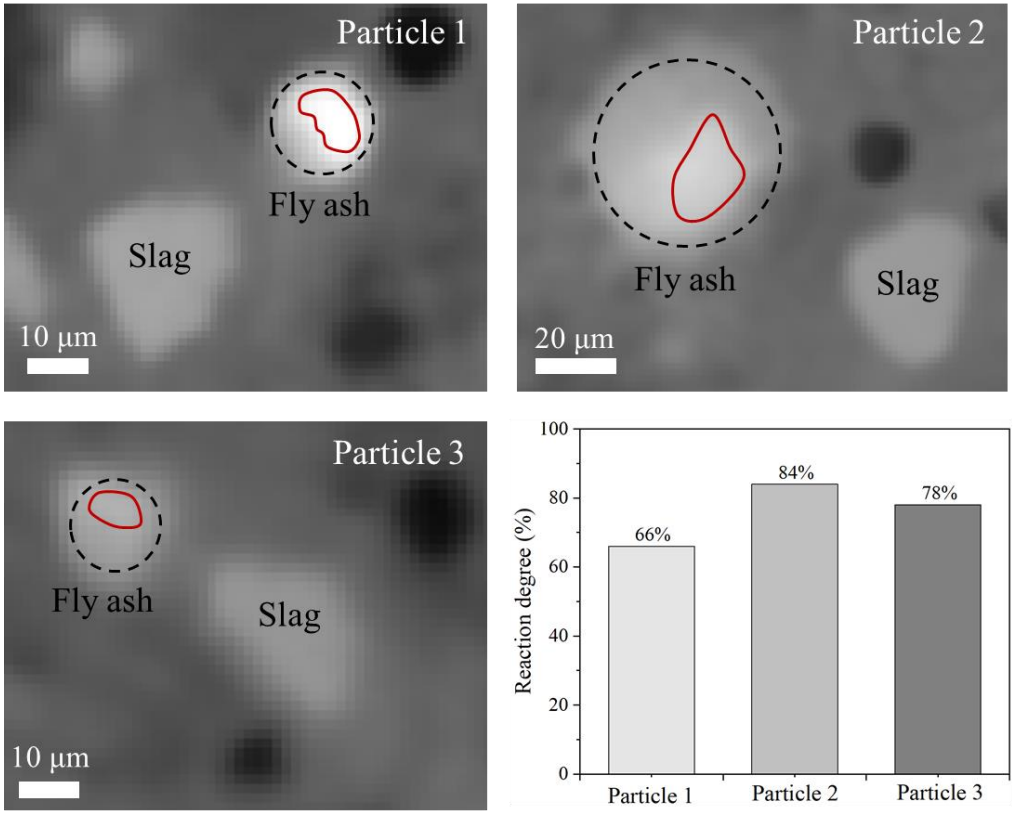

Fig. 23. Reaction degree of fly ash particles near slag particles at 28 d

Table 1. Chemical compositions (wt%) of fly ash and slag

Oxide	SiO_2	Al_2O_3	Fe_2O_3	CaO	K_2O	MgO	TiO_2	Na_2O	SO_3	P_2O_5
Fly ash	55.76	30.22	3.56	2.33	0.91	0.46	1.72	0.40	0.79	0.27
Slag	33.22	13.49	0.40	41.57	0.64	7.04	0.50	0.34	2.14	-

Table 2. Particle size distribution (μm) of fly ash and slag

Cumulative distribution	C_1 (10%)	C_2 (50%)	C_3 (90%)	Average particle size	Median particle size
Fly ash	2	10	32.86	19.06	11.48
Slag	3.08	14.50	36.07	18.98	15.78

Table 3. Mixture quantity of alkali-activated fly ash-slag (AAFS)

	Fly ash	Slag	SS	SH	SP
Weight (kg/m^3)	300	100	120	60	4

Appendix A. Phase segmentation for different fly ash particles

Additional information about the phase identification for different fly ash particles is presented in Table A-1 and Fig. A-1.

Table A-1. Threshold values for phases identification in different fly ash particles

Particle No.	Unreacted fly ash	Inner products	Outer products	Paste matrix
Particle 1 (d_{Eq} = 56.59 μm)	255	255 ~ 175	175 ~ 100	100
Particle 2 (d_{Eq} = 41.30 μm)	153	153 ~ 146	146 ~ 99	99
Particle 3 (d_{Eq} = 28.14 μm)	150	150 ~ 140	140 ~ 100	100
Particle 4 (d_{Eq} = 16.63 μm)	163	163 ~ 152	152 ~ 94	94
Particle 5 (d_{Eq} = 12.93 μm)	233	233 ~ 222	222 ~ 104	104

Note: d_{Eq} is the spherical equivalent diameter.

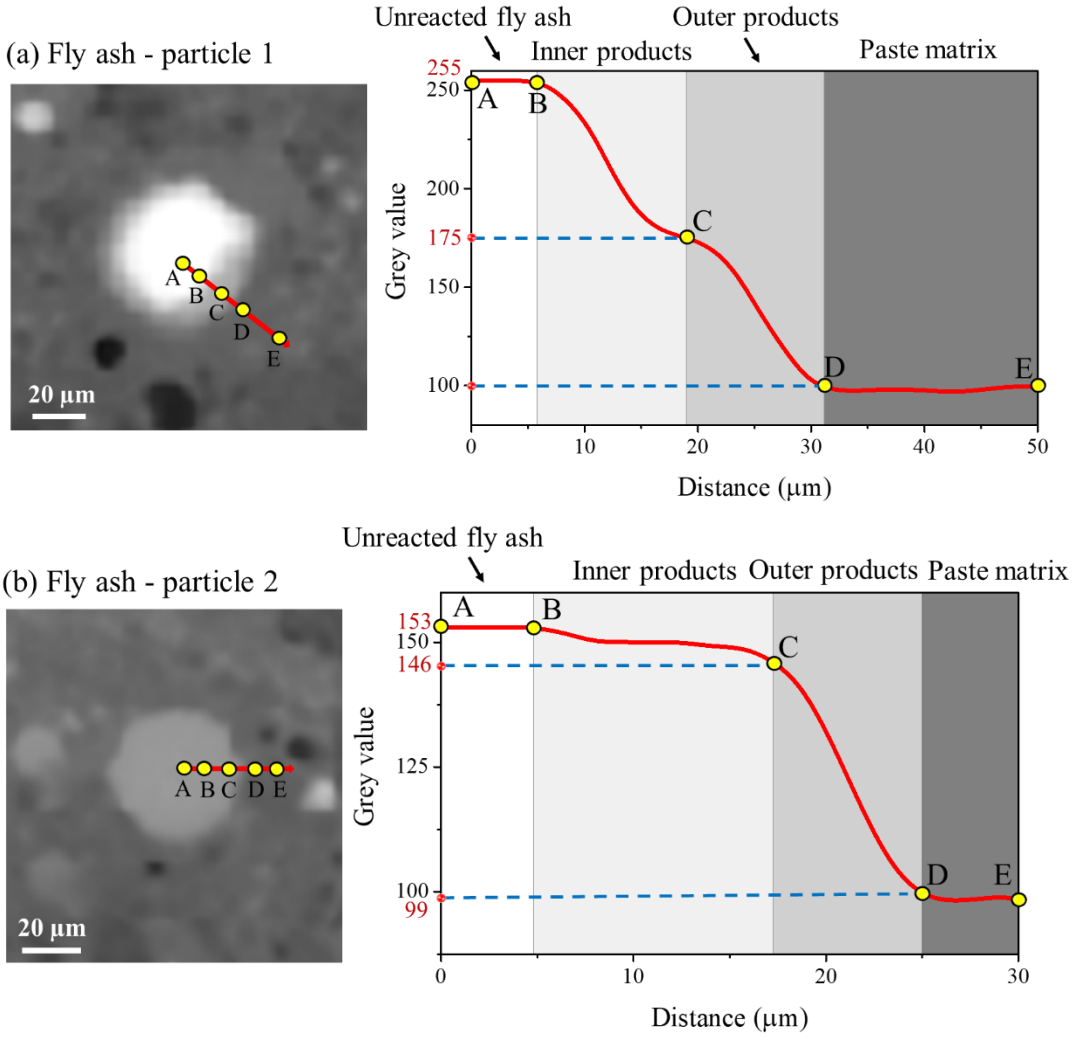

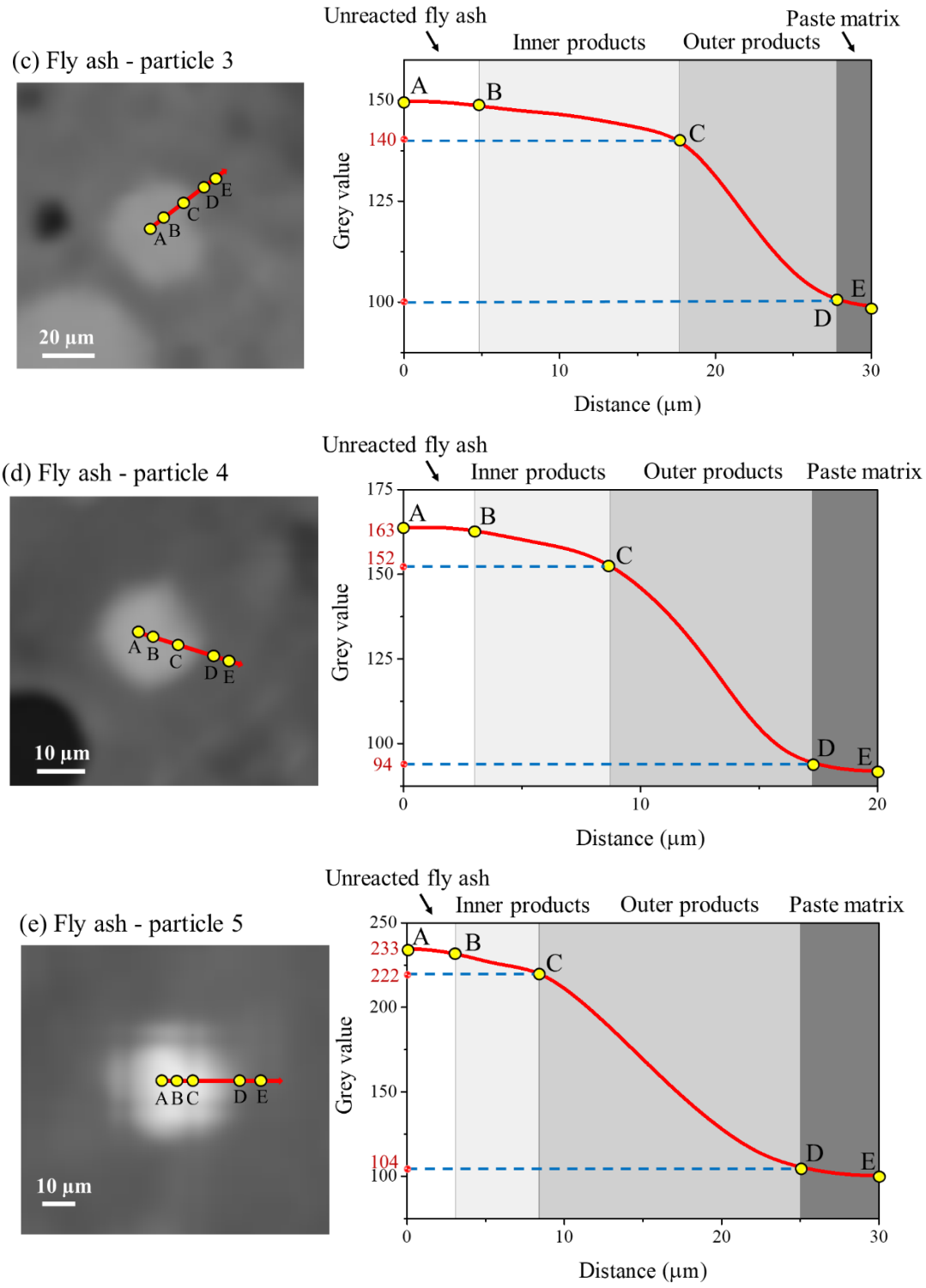

Fig. A-1. Phase identification of different fly ash particles (t = 7 d)

Appendix B. Phase segmentation for different slag particles

Additional information about the phase identification for different slag particles is presented in Table B-1 and Fig. B-1.

Table B-1. Threshold values for phases identification in different slag particles

Particle No.	Unreacted slag	Inner products	Outer products	Paste matrix
Particle 1 (d_{Max}= 74.76 μm)	160	160 ~ 132	132 ~ 94	94
Particle 2 (d_{Max}= 64.22 μm)	203	203 ~ 175	175 ~ 97	97
Particle 3 (d_{Max}= 36.04 μm)	177	177 ~ 165	165 ~ 110	110
Particle 4 (d_{Max}= 21.42 μm)	165	165 ~ 156	156 ~ 110	110
Particle 5 (d_{Max}= 9.48 μm)	150	150 ~ 142	142 ~ 105	105

Note: d_{Maz} is the maximum distance between two points in the original boundary of the central slice.

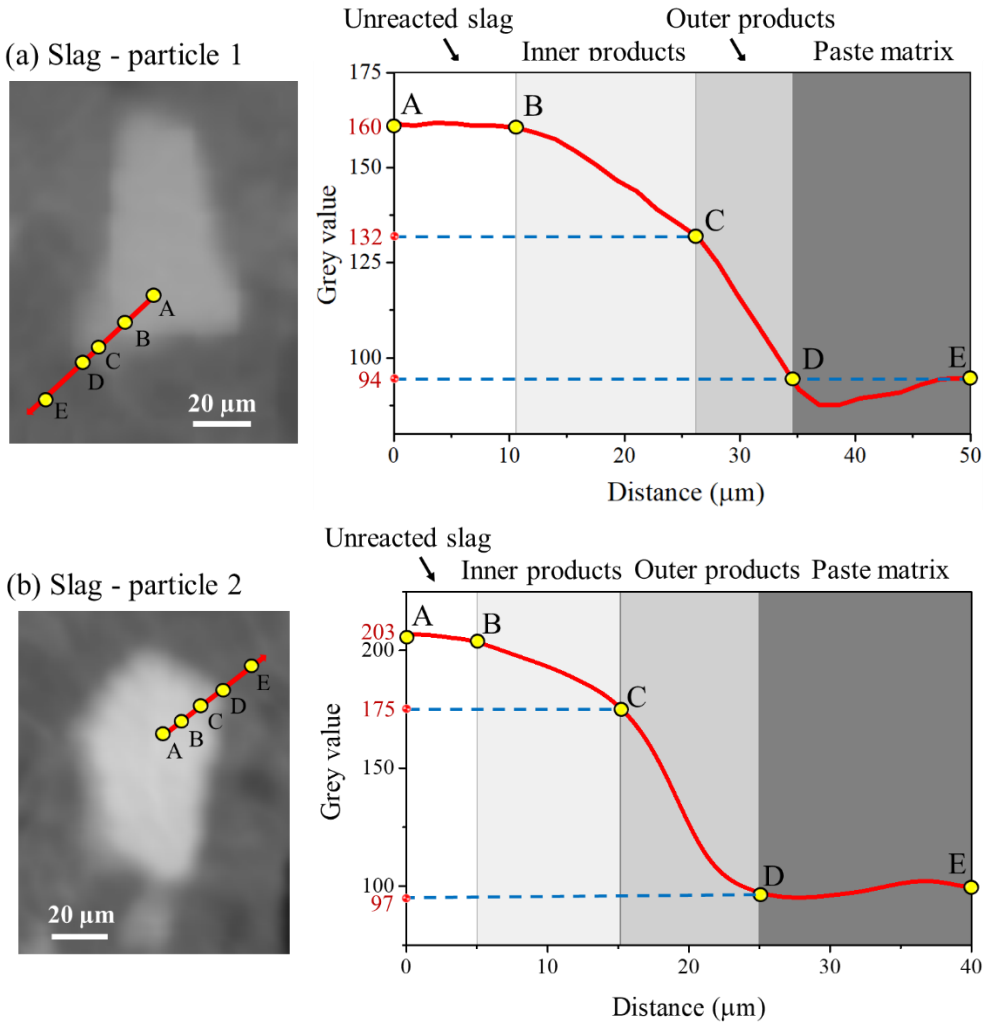

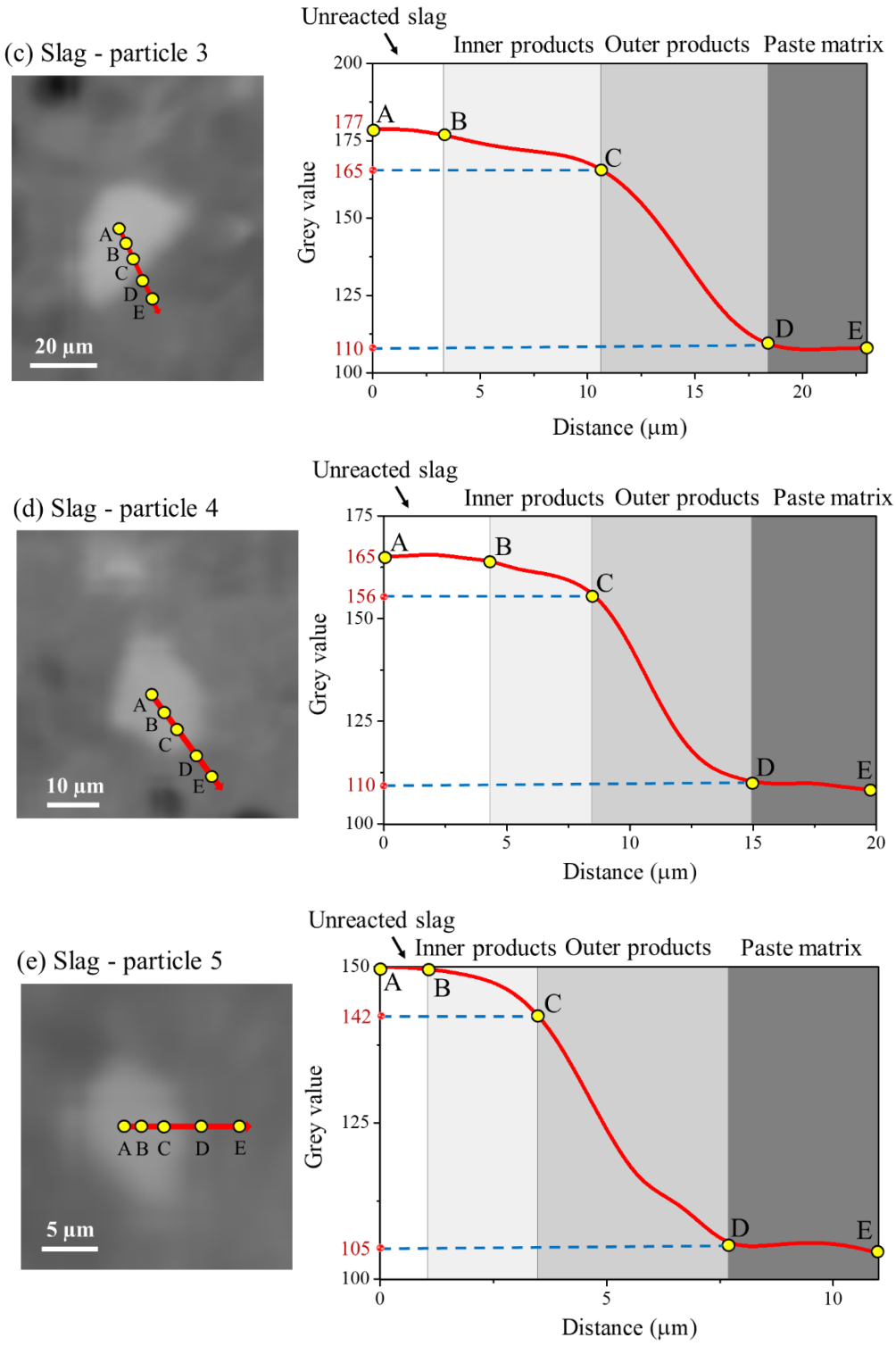

Fig. B-1. Phase identification of different slag particles (t = 1 d)